CrossMark

# Geometrically weighted modal decomposition techniques

**Tso-Kang Wang[1] and Kourosh Shoele[1],†**

[1]Department of Mechanical Engineering, Joint College of Engineering Florida State University-Florida A&M University, Tallahassee, FL 32310, USA

Modal decomposition techniques have become important mathematical methodologies in analysing complex flow physics. The data-driven methods, such as proper orthogonal decomposition and dynamic mode decomposition are used to extract coherent structures in the form of spatial modes. These methods can be applied to both numerical and experimental data to identify the characteristic dynamics of the system. However, the classical data-driven modal decomposition methods are only applicable to problems with a fixed shape and are not suitable for systems with fluid–structure interaction or systems with shape-changing geometries. In this paper we propose a novel method utilizing a conformal mapping technique to solve this issue. Through different examples with deforming geometry, the capability of the method to accurately capture the flow features is demonstrated. The proposed method is found to be suitable for a wide range of applications and a possible candidate for reduced-order flow modelling of complex shape-changing systems.

**Key words:** flow–structure interactions, control theory, low-dimensional models

## 1. Introduction

Fluid flows can be very complex in simple configurations, and the interaction between fluid and structures or the presence of reconfigurable boundaries can further complicate the problem. The nonlinear nature and multiple time scales involved in these problems make it challenging to analyse and dissect the dynamic characteristics of the system (Bazilevs, Takizawa & Tezduyar 2013). In recent years, modal decomposition techniques have shown the potential for extracting critical flow structures from the complex flow fields. However, there are several mathematical and formulation challenges that should be overcome before adopting these techniques to study the flow dynamics of reconfigurable systems. This is the main focus of this paper.

† Email address for correspondence: kshoele@eng.famu.fsu.edu

Modal decomposition is a branch of methods that aim to highlight energetically or dynamically significant features of data (Taira *et al.* 2017). Modal analysis methods have been proposed for different purposes in the past decade, including identifying the linear modal representation of complicated flows. The spatial modes extracted from the flow field, along with their characteristic temporal values, can be used to pinpoint important dynamics, build reduced-order models or develop control strategies. Some modal analysis methods involve discretizing the governing equations to examine the stability of the system (McKeon, Sharma & Jacobi 2013; Jeun, Nichols & Jovanović 2016). Modal analysis methods serve a critical role in modern fluid dynamics research and have been continuously evolving for more challenging problems. Further details can be found in many books and review papers, just to name a few here: Ukeiley *et al.* (2001), Theofilis (2011), Holmes *et al.* (2012) and Kutz (2013), etc.

Two of the most popular modal analysis tools, proper orthogonal decomposition (POD) and dynamic mode decomposition (DMD), share the same characteristic of being data-driven. They both do not need governing equations and are applicable to various disciplines. However, the lack of spatial recognition of the boundaries in these methods poses a problem when they are applied to the problems with moving or deforming geometries. Their spatial modes should be embedded onto a fixed Eulerian space to provide physical representation. However, in many problems, including fluid–structure interaction (FSI) problems, fluid motion often is coupled to deforming or/and vibrating bodies where the geometry is continuously changing. Under such circumstances, without employing a unique geometrical description, the application of the data-driven modal analysis methods is restrained. Different approaches have been proposed to solve this issue.

The fluid-only approaches, wherein the modal analysis is used only within the fluid domain, have been applied to the flow past a pitching foil (Mariappan *et al.* 2013) or a flexible cantilever beam (Cesur *et al.* 2014). It is also utilized to extract the modal content of the wake behind a flexible membrane in experiments (Schmid 2010). Similar techniques are proposed for the structural response and were employed to identify the characteristic pattern of a flapping fish pectoral fin (Bozkurttas *et al.* 2009) and a waving flag (Michelin, Smith & Glover 2008). Although the most important features of structure or fluid are revealed with these methods, the connection between them is not captured. To understand the correlation between the two domains, some research includes both fluid and solid dynamics in the modal analysis. For example, Goza & Colonius (2018) used the combined energy of the fluid and structural phases in constructing POD modes and group the responses of the fluid and structure into a single dataset and employ the DMD technique on them. Liberge & Hamdouni (2010) computed the POD modes by interpolating the time-variant grid to a fixed uniform grid to form a global velocity field. Tadmor *et al.* (2008) leveraged the known periodicity of the system to partition the data and extract the physical harmonic modes. Menon & Mittal (2020*a*) performed DMD to a pitching rigid airfoil by a change of reference frame. However, when these methods are applied to systems involving deforming and/or moving volumetric bodies, certain restrictions are encountered, like the representation of moving interfaces between the fluid and solid requires an infinite number of modes, or the system exhibits non-periodic dynamics preventing the use of any prior knowledge.

Moreover, in many FSI systems, the structural response consists of a few fundamental modes, while the flow response is made up of many dynamically important modes and hidden variables (Blevins 1977; Saffman 1992; Eldredge 2019). The interaction between fluid and solid can persist even at a very small deflection limit of their interfaces. In this situation, the coupled system can be linearized around the mean interface, and the dynamic interactions between two phases can be captured with Eulerian linear models. Still, there

exists another mode of interaction that is accompanied by large changes in the geometry of the solid. This mode interaction is more abundant in the systems with large deformation and extensive reconfiguration capabilities such as flag vibration, bird and insect wings, or fish fins. In many of these systems, repositioning of the interface results in new flow conditions and substantial changes in the interaction forces between the fluid and structure. In this case, to represent the flow with a linear combination of modes, it is necessary to incorporate the geometry changes of the flow domain in the modal analysis and essentially map the problem to a domain with fixed interfaces and bring the effect of mapping function into the governing equations of flow and structure.

In this paper we propose a novel method to combine the conformal mapping technique with the modal analysis. An arbitrary smooth geometry is transformed into a fixed geometry through a unique invertible mapping that preserves many important properties of the flow (Pozrikidis 2011; Eldredge 2019). Conformal mappings preserve angles and form a systematic framework to perform shape analysis of deformable surfaces. They are simple, efficient, energy-invariant and mathematically well-understood procedures with infinitely many derivatives. We focus on two-dimensional systems and express the flow equations based on the vorticity-stream function form in the transformed domain to obtain the flow field on a canonical planar domain for the subsequent data-driven modal analysis. This method provides a natural mapping (as a model of geometric group theory) between a canonical geometry and the real geometry and is applicable to a broad class of smooth geometry. Through examples, the benefit of this method will be shown in the later sections.

The rest of this paper is as follows. In § 2 we first provide an introduction to POD and DMD. We discuss how the proposed method can overcome modal analysis limitations for systems with shape-changing bodies. In § 3 different examples with deforming surfaces are examined to demonstrate how the proposed method can be applied to identify significant flow features. Finally, the conclusion and future direction will be given in § 4.

## 2. Methodology

The basics of the two most popular modal analysis techniques, POD and DMD, will be introduced first. Both of these methods are data-driven and are widely used for various applications. We introduce the proposed method aiming to enable the modal analysis of systems with deforming/moving geometries. The limitations of the proposed method will be reviewed at the end.

### 2.1. *Proper orthogonal decomposition*

The proper orthogonal decomposition technique, also known as the principal component analysis and Karhunen–Loeve transformation, optimally decomposes a complex system into linear combinations of modes. The orthogonal spatial modes acquired from the POD technique capture the most disturbance energy of the flow. Proper orthogonal decomposition was introduced to analyse flow problems first by Lumley (1967), and since then, it has been one of the popular techniques for analysing diverse flow fields. It has numerous applications including but not limited to reduced-order modelling (Aubry *et al.* 1988; Noack *et al.* 2003; Rowley, Colonius & Murray 2004), flow control (Ravindran 2000; Afanasiev & Hinze 2001) and design optimization (LeGresley & Alonso 2000).

The purpose of POD is to form a group of deterministic functions $\phi_i(z)$ that is most similar to the members of a sample function $q(z)$, with $z$ representing the embedded coordinate of the field (Lumley 1967). The notion of 'most similar' is defined by

maximizing the cosine similarity quantity of

$$\frac{\langle q, \phi \rangle}{\|\phi\|_2 \|\phi\|_2}. \tag{2.1}$$

Here the parenthesis $\langle \, , \rangle$ denotes the inner product $\langle f, g \rangle = \int_\Omega f^*(x) g(x) \, dx$, where the asterisk superscript represents both the complex conjugate of a complex scalar and the Hermitian transpose of a vector or tensor, and $\| \cdot \|$ denotes the Euclidean 2-norm. When this normalized inner product is maximized, the function $\phi$ is nearly parallel to a particular characteristic feature of the field $q$. The necessary condition for the optimal linear representation is that $\phi$ should be an eigenfunction of the eigenproblem

$$\int_\Omega \langle q(z), q(z') \rangle \phi(z') \, dz' = \lambda \phi(z). \tag{2.2}$$

Since $R(q(z), q(z')) = \langle q(z), q(z') \rangle$ is compact and bounded, the Hilbert–Schmidt theory guarantees that the eigenproblem has a solution (Lumley 1967). The eigenmodes $\phi_i$ can be ranked according to their eigenvalues $\lambda_i \geq 0$, guaranteed to be larger than 0 due to the non-negative definiteness of $R(q(z), q(z'))$. The eigenvectors are orthogonal and provide complete bases for representing $q$.

For fluid problems, POD is usually applied to the fluctuation of the flow quantities. In the current work we adopt the snapshot POD variant proposed by Sirovich (1987) for its efficiency in handling very high-dimensional problems often encountered in computational fluid dynamics problems. The flow field $u$ is decomposed into spatial modes $\phi_i(x)$ and temporal coefficients $a_i(t)$, i.e.

$$u(\boldsymbol{x}, t) = \bar{u}(\boldsymbol{x}) + u'(\boldsymbol{x}, t) = \bar{u}(\boldsymbol{x}) + \sum_{i=1}^{N} a_i(t) \phi_i(\boldsymbol{x}), \tag{2.3}$$

where $(\bar{\phantom{x}})$ denotes the time-averaging operation. The procedure of applying snapshot POD to a discrete dataset is explained below. For a discrete dataset with $m$ snapshots, the data matrix of $U = \{\boldsymbol{u}'_1, \boldsymbol{u}'_2, \ldots, \boldsymbol{u}'_m\}$ is formed by stacked together $\boldsymbol{u}'_i$, the discrete flow disturbance data of the $i$th snapshot, into a $n \times 1$ vector. The data could be the flow velocity, vorticity or any other quantity of interest. Since $UU^T$ and $U^T U$ have the same set of non-zero eigenvalues, the data structure is examined to decide which combination is a better choice for the eigenvalue calculation. In modern flow applications, the dimension of the acquired dataset from either numerical simulation or an experimental particle image velocimetry system is usually much larger than the number of snapshots. Therefore, oftentimes, it is reasonable to select the covariance matrix as $U^T U$ instead, and solve the eigenvalue problem of

$$U^T U W \psi_j = \lambda_j \psi_j, \quad \psi_j \in \mathbb{R}^m, \quad m \ll n. \tag{2.4}$$

The matrix $W$ here is a weighting matrix accounting for the numerical quadrature and can be constructed for different purposes (Schmidt & Colonius 2020).

The POD modes, $\phi_j$, are defined as the eigenvector of the covariance matrix $UU^T$, and are related to $\psi_j$ by

$$\phi_j = U \psi_j \frac{1}{\sqrt{\lambda_j}} \in \mathbb{R}^n, \quad j = 1, 2, \ldots, m, \tag{2.5}$$

where the eigenvalues $\lambda_j$ represent the energy level of the corresponding POD modes, $\phi_j$. The more popular choices in the flow data are velocity or vorticity, which POD modes are

selected based on their physical representation of the kinetic energy or enstrophy of the flow, respectively. Note that this procedure is essentially equivalent to executing a singular value decomposition (SVD) on the data matrix $U$, with the left-singular matrix containing the orthonormal POD modes. The temporal coefficients can be obtained from

$$a_j = U^T \phi_j, \quad a_j \in \mathbb{R}^m. \tag{2.6}$$

The reconstruction of the snapshots can be performed with a truncated set of POD modes. A simple criterion for deciding the number of required modes $p$ is based on their cumulative representation of the energy or enstrophy, or equivalently, when $\sum_{i=1}^{p} \lambda_i \sim 1$. The truncation of the lower-energy modes are equivalent to denoising the signal, a technique which is extensively used in the fields of signal processing, estimation and pattern recognition (Ly & Tran 2001; Lanata & Del Grosso 2006; Astrid *et al.* 2008). The reconstructed snapshots can be recovered by

$$\tilde{u}_j(t) = \sum_{j=1}^{p} a_j(t) \phi_j. \tag{2.7}$$

Proper orthogonal decomposition modes have several important and unique advantages. They are orthogonal to each other and encode unique aspects of the flow, which is beneficial for constructing an efficient reduced-order model for various flow configurations. Another advantage is that POD distributes the energy of the non-noise part of the signal into the leading POD modes with coherent structures, and, hence, equivalently increases the signal-to-noise ratio. Numerous extensions of the POD technique are developed to overcome different practical and computational challenges. We will introduce some of them that are relevant to the proposed work later in § 2.3.

## 2.2. *Dynamic mode decomposition*

Dynamic mode decomposition, first proposed by Schmid (2010), is another popular and widely used flow analysis technique. It produces a set of spatial modes with corresponding characteristic frequencies and growth/decay rates. The idea behind DMD is to identify the linear harmonic modes which disclose distinct dynamics of a nonlinear system through the eigendecomposition of a best-fit linear operator. The data matrix, defined as $U = \{u_1, u_2, \dots, u_m\}$, is partitioned into two time-consecutive sets $U_{1:m-1} = \{u_1, u_2, \dots, u_{m-1}\}$ and $U_{2:m} = \{u_2, u_3, \dots, u_m\}$. Dynamic mode decomposition seeks to find a constant transition matrix $A$ such that $U_{2:m} \approx A U_{1:m-1}$, subject to minimizing the cost function

$$C = \sum_{i=1}^{m-1} \|u_{2,i} - A u_{1,i}\|^2, \tag{2.8}$$

where $u_{1,i}$ and $u_{2,i}$ are the $i$th columns of the matrices $U_{1:m-1}$ and $U_{2:m}$, respectively. The unique minimum-norm solution of this problem based on the Frobenius norm of $A$ is

$$A = U_{2:m} U_{1:m-1}^+, \tag{2.9}$$

where $U_{1:m-1}^+ = (U_{1:m-1}^* U_{1:m-1})^{-1} U_{1:m-1}^*$ is the Moore–Penrose left inverse of the matrix $U_{1:m-1}$. The eigenvectors of $A$ are defined as the DMD modes, where the frequencies and growth/decay rates are determined from the imaginary and real parts of the eigenvalues.

A computationally efficient technique to calculate DMD modes is introduced by Schmid (2010). This technique is used in this paper. Here, the first step is to compute the reduced SVD of the data matrix

$$U_{1:m-1} = S \, \Sigma \, V^*, \tag{2.10}$$

where $S$ is the left-singular matrix, $\Sigma$ is the singular value matrix and $V$ is the right-singular matrix. We then define the function

$$B \equiv S^* \, U_{2:m} \, V \, \Sigma^{-1} \tag{2.11}$$

and solve the eigenproblem of

$$B \, \tilde{\omega}_j = \tilde{\mu}_j \, \tilde{\omega}_j \tag{2.12}$$

to find the DMD modes as

$$\tilde{\psi}_j = S \, \tilde{\omega}_j. \tag{2.13}$$

The modes $\tilde{\psi}_j$ and eigenvalues $\tilde{\mu}_j$ are acquired from matrix $B$ and are related to that acquired from using matrix $A$ with

$$\psi_j = \tilde{\mu}_j^{-1} \, U_{2:m} V \Sigma^{-1} \, \tilde{\omega}_j, \quad \mu_j = \frac{\log(\tilde{\mu}_j)}{\delta t}, \tag{2.14a,b}$$

where $\delta t$ is the time separation between two consecutive snapshots (Tu *et al.* 2014).

Each DMD mode is a spatial mode indicating a distinct dynamic of the system. These modes are equivalent to a finite-dimensional approximation of the Koopman operators (Rowley *et al.* 2009; Mezić 2013), which map a nonlinear system to an infinite-dimensional linear system. The DMD technique, as Schmid (2010) points out, is not limited to temporal but can also be spatial stability analyses through rearranging the data matrix along the spatial axis of interest.

If the $j$th mode obtained from the DMD approach has a corresponding eigenvalue $\tilde{\mu}_j$, then the frequency and growth/decay rate of this mode can be calculated from

$$f_j = \frac{\text{ang}\left(\tilde{\mu}_j\right)}{2\pi \, \delta t}, \quad d_j = \frac{\log |\tilde{\mu}_j|}{\delta t}, \tag{2.15a,b}$$

where the $\text{ang}(\tilde{\mu}_j)$ is the phase angle of the complex eigenvalue $\tilde{\mu}_j$. The low-rank projected solution can be reconstructed at any time with

$$u_{DMD}(t) = \sum_{k=1}^{K} b_k(0) \, \psi_k \, e^{\mu_j t}, \tag{2.16}$$

where $K$ is the rank of the reduced SVD approximation to $U_{1:m-1}$ and $b_k(0)$ is the initial amplitude of the $k$th mode. The above equation can be represented in matrix form as

$$u_{DMD}(t) = \Psi \, \text{diag}(e^{\mu_j t}) \, b, \tag{2.17}$$

where $\Psi$ is the matrix formed from the DMD modes $\psi$, $\text{diag}(e^{\mu_j t})$ is a diagonal matrix with $e^{\mu_j t}$ as entries and $b$ is a vector calculated by

$$b = \Psi^+ x_1, \tag{2.18}$$

where $x_1$ is the initial snapshot and $b$ is a vector formed from $b_k(0)$.

The above algorithm is one of the common definitions of DMD modes. As Tu *et al.* (2014) point out, there are multiple different definitions of DMD modes and each definition

provides a different perspective of the system dynamics. Dynamic mode decomposition is capable of isolating specific dynamics in the system according to their frequencies. It is data-driven and can be expanded with mathematical tools for numerous applications. Compared with POD, DMD modes are not orthogonal to each other and have no differentiation in eigenvalue importance, but they can reveal critical dynamic information of the system.

### 2.3. *Geometrically weighted modal decomposition*

The commonly used snapshot POD and classical DMD both produce spatial Eulerian modes, whereas the temporal effects are incorporated in their temporal coefficients or eigenvalues. Different variants of the POD and DMD methods have been proposed to expand the capabilities of these methods (Holmes *et al.* 2012; Kutz 2013; Taira *et al.* 2017).

One of the usual difficulties of the popular snapshot POD is that while their resultant modes are energetically optimal, they might fail to capture critical system dynamics. The spectral POD proposed by Towne, Schmidt & Colonius (2018) finds modes that depend on both space and time by extending the stochastic ensemble from snapshots of a flow field to a collection of realizations of the time-dependent flow. Another method with the same name (Sieber, Paschereit & Oberleithner 2016) applies a filter to the correlation matrix such that the stochastic fluctuations are attenuated while leaving the coherent structures unaffected. The sequential POD (Jørgensen, Sørensen & Brøns 2003) collect multiple sets of snapshots with different parameter settings to ensure that the dynamically important data are better represented in the extracted modes. Also, POD techniques have been extended to incorporate available information about the importance of modes as a weighting function in Bayesian methods such as the probabilistic principle component analysis (PCA) (Tipping & Bishop 1999) or sensible PCA (Moghaddam & Pentland 1995; Roweis 1998).

Modified DMD methods have been developed to improve certain shortcomings of the classical DMD approach. For example, the streaming DMD (Hemati, Williams & Rowley 2014) can update the DMD computations incrementally with a number of orthogonal basis vectors, windowed DMD (Zhang *et al.* 2019) permits the frequency change in the system by placing less weight on older snapshots, and multiresolution DMD (Kutz, Fu & Brunton 2016) recursively isolates the lower-rank modes of the system to separate the important dynamics with distinct scales.

However, lots of FSI systems such as fish swimming (Liu, Wassersug & Kawachi 1996), flapping wings (Takizawa *et al.* 2012), heart valves (Kamensky *et al.* 2015) or wind turbines (Hsu & Bazilevs 2012) have moving or deforming volumetric structures with large deformation. As most of the modal analysis techniques are data-driven, their spatial description must remain time invariant for the modes to capture physically significant features of the flow. When there is a large deformation body in the flow, immersed interface techniques (Mittal & Iaccarino 2005) with a fixed grid or a body-fitted time-varying coordinate system (Connell & Yue 2007) can be employed to study the flow dynamics computationally. In the former group, to capture the moving interface, an infinite number of modes are needed, akin to how infinite Fourier modes are required to rebuild a step function. For the latter case, the spatial modes acquired from the modal analysis do not have a fixed spatial grid to embed on and are hence uninterpretable. Suppose the data-driven techniques like POD and DMD are to be employed to understand the flow physics in these applications, in that case, a mathematical framework is necessary for efficiently and accurately transforming a time-variant fluid domain into a time-invariant one with minimal changes to the flow equations. The proposed geometrically weighted

modal decomposition techniques combine a proper transformation and the modal analysis to tackle the spatial embedding problem.

### 2.3.1. *Conformal mapping and body-fitted grids*

To describe the fluid dynamics around a moving and deforming structure, we employ a body-fitted mesh and the finite difference approach. The grid is generated with a well-established conformal mapping technique (Pozrikidis 2011; Eldredge 2019), which can be deployed upon any arbitrary smooth shape to transform the geometry into a canonical shape, e.g. a cylinder with a specified diameter. The choice of the transformation is a critical aspect of calculating the physically relevant geometric weighting function for the modal analysis procedures.

We assume that the shape of an arbitrary object can be represented with a series of sufficiently smooth contour curves in the Cartesian space. The procedure, following Pozrikidis (2011), is as follows.

(i) The contour boundary of the body is traced with $N$ points. The coordinates of the points are represented as $z_j = x_j + iy_j$ numbered in the counterclockwise direction for $j = 1, \ldots, N$.

(ii) Here we choose to map the exterior of the body to the exterior of a circle with the radius $\lambda$ centred at the origin. The computational grid is constructed based on the cylindrical coordinate around the circle defined as $\zeta = \lambda e^{i\phi}$, with $\phi$ being the polar angle. The relation between $\lambda$, $\phi$ and $z$ can be expressed with the Laurent series expansion

$$z(\phi) = \lambda e^{i\phi} + a^0 + \sum_{n=1}^{\infty} a^n e^{-in\phi}. \qquad (2.19)$$

(iii) The radial distance $\lambda$ and the series coefficients $a^n$ are calculated with the use of the orthogonality properties of $e^{-in\phi}$ kernel,

$$\lambda = \frac{1}{2\pi} \int_0^{2\pi} [x(\phi)\cos(\phi) + y(\phi)\sin(\phi)]\, d\phi, \qquad (2.20)$$

$$\mathrm{Re}[a^n] = \frac{1}{2\pi} \int_0^{2\pi} [x(\phi)\cos(n\phi) - y(\phi)\sin(n\phi)]\, d\phi, \qquad (2.21)$$

$$\mathrm{Im}[a^n] = \frac{1}{2\pi} \int_0^{2\pi} [x(\phi)\sin(n\phi) + y(\phi)\cos(n\phi)]\, d\phi. \qquad (2.22)$$

(iv) The coordinates $z(\phi)$ are expressed on the Cartesian plane for selected values of $\lambda$ and $\phi$, and compared with the original contour curve. The values $\phi_i$ are then optimized through minimization of $L^2$-norm of the error,

$$\|\Delta z_i\|^2 = (x_i - x(\phi_i))^2 + (y_i - y(\phi_i))^2. \qquad (2.23)$$

As an example, the conformal grid for an energy efficient transport (EET) high-lift airfoil with an attached flap generated from this algorithm along with the cylindrical grid in $\zeta$ plane are shown in figure 1. The grid is also strained logarithmically in the radial direction with more resolution near the surface to accurately capture the unsteady aerodynamic effects.

The most important advantage of this procedure for the modal decomposition is that the transformed domain in the $\zeta$-plane is time invariant. In general, the computational grid
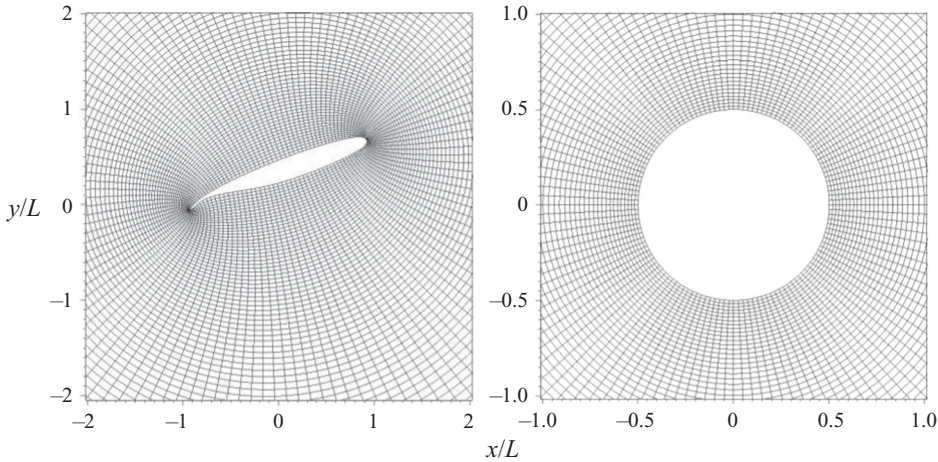
Figure 1. Computational grid in the physical domain around an EET high-lift airfoil and the transformed domain around a unit circle.

of the transformed domain is designed to resolve the space where most dynamics happen, or where the geometry has its most temporal variations. The conformal mapping mainly expands the region next to the surface where fine flow details are present and, thus, results in better identification of such flow features. Note that the conformal mapping process does not change the value of the independent variables embedded in the spatial grid; thus, the mapping effectively redistributes the independent variables in space. In this paper, the distribution of the points along the contour curve is determined by the local surface curvature. The technique also sets up the fixed grid required for POD, DMD and other spatial modal decomposition methods. More discussion about this aspect will be given later in this section.

### 2.3.2. *Governing flow equations*

The flow dynamics around the structure is solved in the transformed domain $\zeta = r e^{i\phi}$ using the modified Navier–Stokes equation incorporating the effect of the conformal transformation. The Navier–Stokes equations are expressed in the vorticity-stream function $(\omega - \psi)$ form as

$$\frac{\partial \omega}{\partial t} + \frac{1}{\sqrt{|J|}} \left[ v_r \frac{\partial \omega}{\partial r} + \frac{v_\theta}{r} \frac{\partial \omega}{\partial \theta} \right] = \frac{1}{Re\,|J|} \left[ \frac{\partial^2 \omega}{\partial r^2} + \frac{1}{r} \frac{\partial \omega}{\partial r} + \frac{1}{r^2} \frac{\partial^2 \omega}{\partial \theta^2} \right], \qquad (2.24)$$

$$\frac{\partial^2 \psi}{\partial r^2} + \frac{1}{r} \frac{\partial \psi}{\partial r} + \frac{1}{r^2} \frac{\partial^2 \psi}{\partial \theta^2} = -|J|\omega, \qquad (2.25)$$

where $Re$ is the Reynolds number, $|J|$ is the determinant of the Jacobian of the transformation $\zeta = \xi + i\eta \Rightarrow z = x + iy$, and $v_r$ and $v_\theta$ are the transformed velocities which incorporate time-dependent effects of the mapping process. Because the independent variables like the vorticity do not change during the conformal mapping process, we can recover the desired flow data with the reverse mapping from the solution obtained in the transformed domain. A similar procedure using Joukowski transformation can be found in Guglielmini & Blondeaux (2004) and Zhu & Peng (2009). Further detail of the formulation is provided in appendix B.

### 2.3.3. *Fluid–structure interaction*

Aside from the geometry change, the current algorithm also embodies the translational and rotational motions of the structure, denoted with the heaving distance $h$ and pitching angle $\alpha$, respectively. For the FSI problem in § 3.3, the body motion is modelled by connecting the structure to a set of linear and torsional dampers and springs with damping and stiffness coefficients $c_{h/\alpha}$ and $k_{h/\alpha}$, respectively. The structural motions are related to the fluid forces and torques by the equations of motion

$$\begin{bmatrix} m & S_\alpha \\ S_\alpha & I \end{bmatrix} \begin{bmatrix} \ddot{h} \\ \ddot{\alpha} \end{bmatrix} + \begin{bmatrix} c_h & 0 \\ 0 & c_\alpha \end{bmatrix} \begin{bmatrix} \dot{h} \\ \dot{\alpha} \end{bmatrix} + \begin{bmatrix} k_h & 0 \\ 0 & k_\alpha \end{bmatrix} \begin{bmatrix} h \\ \alpha \end{bmatrix} = \begin{bmatrix} F_{fluid} \\ M_{fluid} \end{bmatrix}, \qquad (2.26)$$

where $m$ is the mass of the body and $S_\alpha$ and $I$ are the static imbalance and moment of inertia, respectively.

The fluid and the structural equations are solved using a tightly coupled algorithm with the following steps.

(i) At time step $n$, the heaving motion $\dot{h}_{n-1}$ and pitching motion $\dot{\alpha}_{n-1}$ from the last time step are used as the initial values for solving FSI problem at time $n$.

(ii) The hydrodynamic forces and moment are calculated based on the current value of $\dot{h}$ and $\dot{\alpha}$.

(iii) We update $\dot{h}_n$ and $\dot{\alpha}_n$ with the calculated hydrodynamic forces and moment exerted on the airfoil.

(iv) The iteration between the fluid and foil dynamics repeats until $\dot{h}_n$ and $\dot{\alpha}_n$ converge, then the algorithm progresses to the next time step.

The Navier–Stokes equations are discretized in $r$, $\theta$ and $t$. For the vorticity transportation equation, a central difference scheme with second-order accuracy is implemented. For time integration, the vorticity field is updated at each time step via an alternative direction implicit technique. Two boundary conditions are imposed: on the structure surface, the no-slip boundary condition is enforced, and the free stream velocity is specified at the far-field boundaries. The Poisson equation is solved using a semi-spectral method, wherein the Fourier transformation is employed along $\theta$, and the finite difference technique is used along $r$. The validation of the algorithm is presented in appendix A.

### 2.3.4. *Modal analysis*

The algorithm introduced above is capable of modelling the flow dynamics of a system with arbitrary smooth shape-changing bodies. Through the conformal mapping procedure, the system now resides on a time-invariant grid. This resolves the aforementioned problem of spatial recognition when applying classical modal analysis techniques to FSI systems involving a deforming/moving volumetric body. The conformal mapping enables the modal analysis to be applied to such a system by weighting the spatial distribution of the flow data based on the geometry in the physical domain and, thus, is named as geometrically weighted modal decomposition (GW-MD). However, since the conformal mapping process transforms the time-dependent structural domain to a fixed shape, the modes obtained from GW-MD are now spatio-temporal modes. Some questions arising from this procedure would be: what temporal effects have been incorporated in these modes? How does the transformation change the POD or DMD modes, and how should we interpret them? We will discuss these questions next.

First, let us consider how the mapping process changes the physical properties of the modes. In the transformed $\zeta$ domain, the grid is time invariant, and we can employ modal

analysis techniques to get the spatial modes. When an inverse mapping is applied to project the modes to the original $z$ domain, temporal effects are introduced through the Jacobian $\boldsymbol{J}$ of $\zeta = \xi + i\eta \Rightarrow z = x + iy$ transformation, with the metric of the transformation being

$$|J|(t) = \frac{\partial x(t)}{\partial \xi} \frac{\partial y(t)}{\partial \eta} - \frac{\partial x(t)}{\partial \eta} \frac{\partial y(t)}{\partial \xi}, \tag{2.27}$$

wherein the $x$ and $y$ are the time-varying physical position of a particular point in the physical domain. Therefore, the Jacobian is also time variant. It follows that

$$\mathrm{d}\vec{z} = |J| \, \mathrm{d}\vec{\zeta} \quad \text{and} \quad \boldsymbol{\nabla}_z = \boldsymbol{J}^{-1} \cdot \boldsymbol{\nabla}_\zeta, \tag{2.28a,b}$$

and based on the mapping properties,

$$\boldsymbol{J}^{-1} = \frac{1}{|J|} \boldsymbol{J}^{\mathrm{T}}. \tag{2.29}$$

The Jacobian serves as a spatial weighting originating from the conformal mapping procedure; hence, called the geometric weighting. To illustrate how this weighting affects the outcome of the POD modes, we take the velocity and vorticity as examples. From (2.2) we know that the POD modes are the solution to the eigenproblem. This inner product in the transformed domain $\Omega_\zeta$ defines how the geometric mapping affects the modes.

(i) Velocity: the inner product of the velocity in the physical and transformed domains are related through

$$R(v, v) = \langle v, v \rangle = \int_{\Omega_\zeta} v^*(z) v(z) \, \mathrm{d}\zeta = \int_{\Omega_\zeta} (\boldsymbol{\nabla}_\zeta \times \psi)^* (\boldsymbol{\nabla}_\zeta \times \psi) \, \mathrm{d}\zeta$$

$$= \int_{\Omega_z} (\boldsymbol{J} \cdot \boldsymbol{\nabla}_z \times \psi)^* (\boldsymbol{J} \cdot \boldsymbol{\nabla}_z \times \psi) \frac{1}{|J|} \, \mathrm{d}z = \int_{\Omega_z} (\boldsymbol{\nabla}_z \times \psi)^* (\boldsymbol{\nabla}_z \times \psi) \, \mathrm{d}z. \tag{2.30}$$

The conformal transformation hence preserves the kinetic energy. This is because of a specific relation between the role of mapping on the dilatation term and gradient operator. As a result, for stationary objects, modes acquired in the transformed domain are the exact modes obtained in the physical domain based on the kinetic energy. We should emphasize that currently there is no proper way to perform POD in the actual physical domain due to the moving structures. Through the conformal mapping we merge the structural effect into the governing equation and the POD modes acquired in the transformed domain incorporate the solid movement into the flow. Geometrically weighted proper orthogonal decomposition (GW-POD) modes are, therefore, hybrid modes in nature and act as lifting operators (Marsden 1981).

To demonstrate that the energy content is the same in the transformed and physical domains, we look at a stationary airfoil submerged in an ambient flow. Proper orthogonal decomposition is performed in both the transformed and physical domains with the velocity in the respective domain. The velocity in the transformed domain for a stationary geometry, based on (B20) and (B21), is defined as

$$v_\xi = \frac{1}{\sqrt{|J|}} \frac{\partial \psi}{\partial \eta}, \quad v_\eta = \frac{-1}{\sqrt{|J|}} \frac{\partial \psi}{\partial \xi}. \tag{2.31a,b}$$

The projection process is simple to carry out for stationary geometry cases since the operator $\boldsymbol{\nabla}_\zeta$ does not include any time-dependent effect. The velocity modes in the two
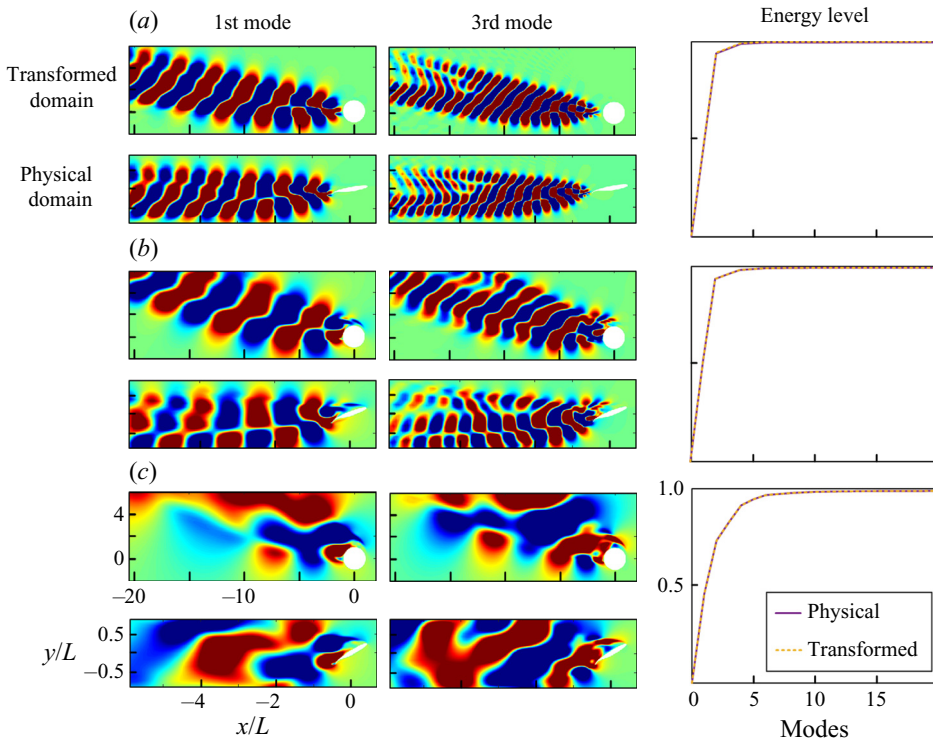
Figure 2. The first and third velocity POD modes and the normalized accumulative energy level in the transformed and physical domain of an airfoil with (*a*) 10°, (*b*) 20° and (*c*) 30° angles of attack. For simplicity, the duplicate axis indices are not present.

domains are related through

$$u = \frac{\partial \psi}{\partial y} = \sqrt{|J|} \left( v_\xi \frac{\partial \eta}{\partial y} - v_\eta \frac{\partial \xi}{\partial y} \right), \quad v = -\frac{\partial \psi}{\partial x} = \sqrt{|J|} \left( -v_\xi \frac{\partial \eta}{\partial x} + v_\eta \frac{\partial \xi}{\partial x} \right).$$
$$(2.32a,b)$$

For simplicity, we only show the horizontal velocity component in figure 2. For all three cases with different AoA, the accumulative energy curves are identical across two different domains. As shown in figure 3, the modes are also found to be similar, proving the energy conservation nature of the conformal mapping process. In fact, the individual modes also contain the same energy content. An extra $J^{\mathrm{T}}J$ term is cancelled out with the domain expansion and contraction through the mapping process. This guarantees that the contribution of eigenvalues stays the same after the transformation. Therefore, the energy captured by each mode is also conserved. We will talk about how the mapping process affects the modal analysis performed with the vorticity next.

(ii) Vorticity: we start by inspecting the inner product:

$$R(\omega, \omega) = \langle \omega, \omega \rangle = \int_{\Omega_z} \omega^*(z)\omega(z)\, \mathrm{d}z = \int_{\Omega_\zeta} \omega^*(\zeta)\omega(\zeta)|J|\, \mathrm{d}\zeta. \qquad (2.33)$$

Since the vorticity remains the same at corresponding locations through the mapping process, the same procedure brings forward an extra Jacobian term in the correlation factor.
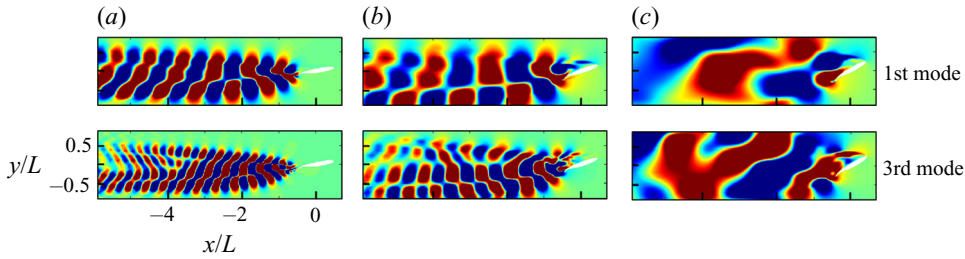
**911** A41-12

Figure 3. The velocity POD modes of an airfoil with (*a*) 10°, (*b*) 20° and (*c*) 30° angle of attack acquired in the transformed domain mapped to the physical domain. These modes are identical to the modes acquired in the physical domain in figure 2.

To recover the enstrophy in the physical domain, we can adopt a new definition of the geometrically weighted inner product:

$$R_{GW}(v_1, v_2) = \langle \boldsymbol{J} \cdot v_1, \boldsymbol{J} \cdot v_2 \rangle_{GW}$$

$$= \int_{\Omega_{GW}} (\boldsymbol{J} \cdot v_1(z))^* (\boldsymbol{J} \cdot v_2(z)) \, \mathrm{d}z = \int_{\Omega_{GW}} v_1^*(z) v_2(z) \, |J| \, \mathrm{d}z. \qquad (2.34)$$

We will check if this modified product satisfies the principle definition of the inner product next. A vector space V with underlying field $\mathbb{R}$ or $\mathbb{C}$ is known as an inner product when operation $\langle \, , \rangle$ satisfies the following conditions.

(*a*) Symmetry: for all vectors $v_1$ and $v_2$, $\langle v_1, v_2 \rangle = \overline{\langle v_2, v_1 \rangle}$.
(*b*) Linearity: for any scalar $a$ and all vectors $v_1$, $v_2$ and $v_3$, $\langle av_1, v_2 \rangle = \bar{a}\langle v_1, v_2 \rangle$ and $\langle v_1, v_2 + v_3 \rangle = \langle v_1, v_2 \rangle + \langle v_1, v_3 \rangle$.
(*c*) Positive-definiteness: for any vector $v$, $\langle v, v \rangle \geq 0$ and that $\langle v, v \rangle = 0$ implies that $v = 0$.

Now let us inspect if the product $R_{GW}(v_1, v_2)$ satisfies these properties.

(*a*) Symmetry:

$$R_{GW}(v_1, v_2) = \langle \boldsymbol{J} \cdot v_1, \boldsymbol{J} \cdot v_2 \rangle_{GW} = \int_{\Omega_{GW}} v_1^*(z) v_2(z) \, |J| \, \mathrm{d}z = \overline{\langle \boldsymbol{J} \cdot v_2, \boldsymbol{J} \cdot v_1 \rangle}_{GW}.$$
$$\qquad (2.35)$$

(*b*) Linearity:

$$R_{GW}(av_1, v_2) = \langle \boldsymbol{J} \cdot av_1, \boldsymbol{J} \cdot v_2 \rangle_{GW} = \int_{\Omega_{GW}} (av_1(z))^* \, v_2(z) \, |J| \, \mathrm{d}z$$

$$= \bar{a} \int_{\Omega_{GW}} v_1^*(z) \, v_2(z) \, |J| \, \mathrm{d}z = \bar{a}\langle \boldsymbol{J} \cdot v_1, \boldsymbol{J} \cdot v_2 \rangle_{GW}, \qquad (2.36)$$

$$R_{GW}(v_1, v_2 + v_3) = \langle \boldsymbol{J} \cdot v_1, \boldsymbol{J} \cdot (v_2 + v_3) \rangle_{GW} = \int_{\Omega_{GW}} v_1^*(z)(v_2 + v_3)(z) \, |J| \, \mathrm{d}z$$

$$= \int_{\Omega_{GW}} v_1^*(z) v_2(z) \, |J| \, \mathrm{d}z + \int_{\Omega_{GW}} v_1^*(z) v_3(z) \, |J| \, \mathrm{d}z$$

$$= \langle \boldsymbol{J} \cdot v_1, \boldsymbol{J} \cdot v_2 \rangle_{GW} + \langle \boldsymbol{J} \cdot v_1, \boldsymbol{J} \cdot v_3 \rangle_{GW}. \qquad (2.37)$$

**911** A41-13

(*c*) Positive-definiteness:

$$R_{GW}(v, v) = \langle \boldsymbol{J} \cdot v, \boldsymbol{J} \cdot v \rangle_{GW} = \int_{\Omega_{GW}} v^*(z) v(z) |J| \, \mathrm{d}z \geq 0. \qquad (2.38)$$

We see that the new definition satisfies all three criteria and, thus, represents a proper energy form that combines the flow energy and the structure motion with a proper weighting function. The key to this is that a conformal mapping always provides a positive Jacobian determinant. There is no fold-over in the mapping process, and the angle and topology are preserved. The geometric weighting is hence not arbitrary but coming from a unique transformation. For the scenarios in which weighting is not desirable, such as when the far-field flow feature is of primary interest, with a simple modification of the inner product, the effect can be removed from the modes.

In figure 4 we provide examples with static geometry to illustrate this unique property of the mapping. We perform POD analysis of an airfoil with a $20°$ angle of attack in different settings: with and without the Jacobian modification. The modes acquired with the modified inner product $R_{GW}$ are denoted as the 'physical-domain' modes as the weighting counterbalance the mapping effect. When POD is performed in the near-body region, the modes and the accumulative enstrophy curves with or without the Jacobian modification are mostly the same. However, in the full-field modal analysis, the mode shapes show some differences in the wake, which result from the grid area expansion in the downstream location. Interestingly, the accumulative enstrophy curves are nearly identical in near-body and full-field cases, indicating that most of the enstrophy aggregates in the near-body region in this case.

Applying weights to data in order to emphasize the important aspect of a system can be seen in several previous works. For example, the weighted POD (Christensen, Brøns & Sørensen 1999) and sequential POD (Jørgensen *et al.* 2003) assign weights to the snapshots to detect the low energetic yet dynamically important modes. The phase-invariant POD (Fogleman *et al.* 2004) stretches the velocity field in one direction to bring the POD modes to the same configuration, which a similar strategy is also used for a backward-facing ramp (Taylor & Glauser 2004). The proposed method here offers a systematic weighting function through the unique benefit of the conformal mapping, and if necessary, the users can recover the physical-domain enstrophy with the modified inner product.

On the other hand, the DMD modes represent the dynamics with specific characteristic frequencies. In the proposed method, $A$ or $B$ matrices identify how the system evolves over time in the transformed space. The conformal mapping provides a time-invariant frame for the spatial modes to embed on in the transformed space. The deforming or moving body in the fluid can be seen as a sharp boundary sweeping through the fluid domain, and approximating such motion in the Eulerian domain requires an infinite number of linear modes. The GW-MD instead integrates the nonlinear effect into a Laplacian-conserved mapping between domains to avoid the problem.

The method described above shows several significant benefits. First, based on the uniformization theorem, there is a conformal connection between any simply connected Riemann surface with one of three canonical shapes of the unit disk, the complex plane or the Riemann sphere. Hence, there is no restriction to the geometries other than being smooth. Secondly, it does not demand an additional definition of energy or prior knowledge of the system. Also, all the available extended versions of the modal analysis techniques, such as the aforementioned online DMD or multiresolution DMD (mrDMD), can be readily deployed. The proposed method is also applicable to both experimental and computational data provided the geometry contour is available. In those cases,
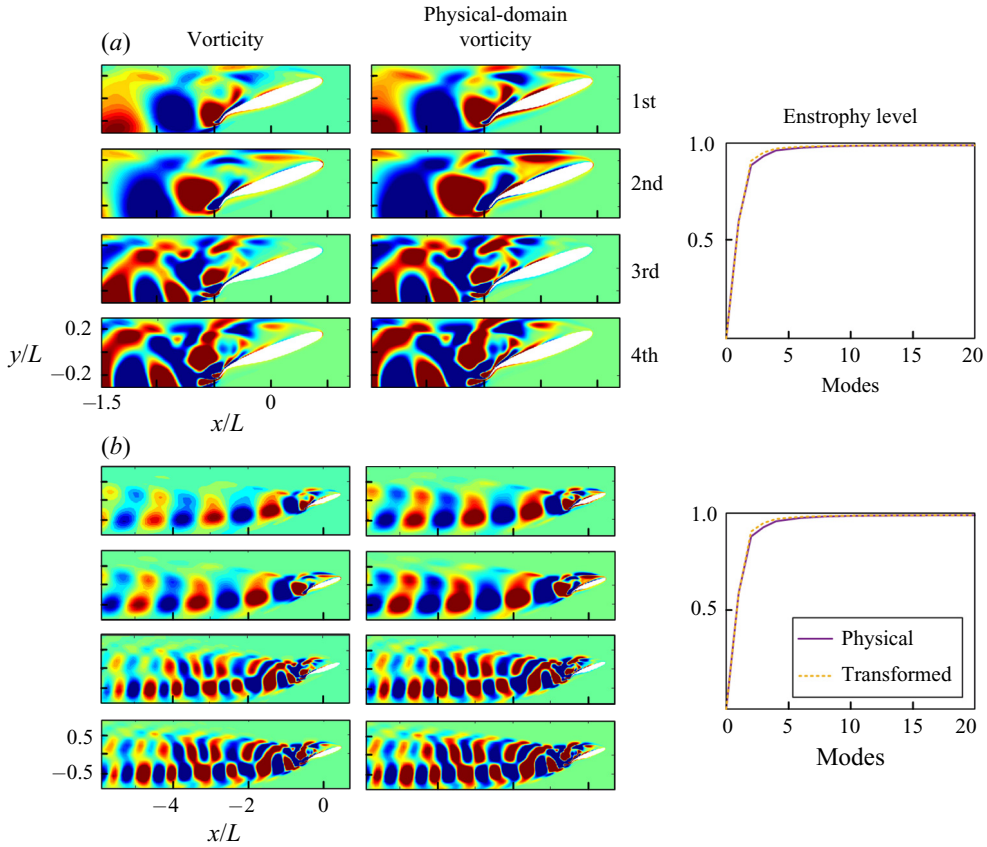
Figure 4. The vorticity POD modes and accumulative normalized enstrophy level of an airfoil with $AoA = 20°$ within (*a*) the near-body field and (*b*) an extended region, including further downstream.

the conformal mapping procedure can be applied in post-processing modal analysis. A similar idea of post-applying modal analysis techniques is suggested by Troshin *et al.* (2016) and tested on a set of heaving airfoil results.

Reduced-order modelling can also benefit from the modal analysis. One of the advantages of POD modes is that they form optimal orthogonal bases to reduce the governing equations into sets of ordinary differential equations with techniques such as the Galerkin projection. Through this procedure, the nonlinear system can be approximated with a reduce-order model (ROM) that could represent the original system with adequate accuracy. Nevertheless, for systems with deforming or moving boundaries, the lack of a proper technique to obtain POD modes restricts the ROM development. Anttonen, King & Beran (2003) looked at a case of potential flow over an oscillating panel by performing POD on a deforming grid, which is generated by holding the same grid number in the vertical direction. Freno & Cizmas (2014) further explored the problem using a dynamic average base flow and basis functions and showed that this method can recover the flow features better than standard snapshot POD modes. Liberge & Hamdouni (2010) proposed the multiphase POD method to extend the Navier–Stokes equations to the solid domain by using a penalization method and indicated its effectiveness in reconstructing flow over an oscillatory cylinder. The proposed method is in line with the principle of these previous techniques, with the

main difference that here the solid motion is systematically lifted and embedded into the governing flow equations in a fixed domain such that it preserves important flow properties. It can also equivalently be formulated as a partial differential equation constraint mapping method in the celebrated topological manifold submersion and immersion techniques in differential topology (Lang 2012). If the deformation of the surface is accessible, one can form ROMs of the flow dynamics using the GW-POD modes. One shortcoming of the proposed method is the lack of information about the solid internal dynamic in the process of developing the ROM in the reference domain. A potential remedy is to extend the mapping with a proper complementary energy function for the solid deformation to obtain the hybrid flow-solid POD modes concurrently (Goza & Colonius 2018). An alternative technique is to identify the POD modes of the deformable geometries in their Lagrangian domains and employ their reconstructed surface motion to form a ROM of the flow dynamics. This method is particularly suitable for FSI problems in which the time scales of the solid domain are narrow-band imposed by its natural frequencies while the flow includes a broad range of dynamically important frequencies.

A limitation of the proposed method is that it is restricted to two-dimensional systems since conformal mapping primarily exists for two-dimensional space. For general two dimensional embedded surfaces in three-dimensional (3-D) space, techniques such as Riemann mapping, cone singularities, Cauchy–Riemann equation, Ricci flow or Dirac equation can be employed to form the conformal mapping between two arbitrary surfaces. The extension of a full conformal mapping to higher dimensions is only feasible through Mobius transformation according to Liouville's theorem (Flanders 1966). However, many quasi-conformal techniques are still available to form a flexible 3-D mapping between volumes with minimal distortion from fully conformal mapping (Hurdal *et al.* 1999; Gu *et al.* 2004; Li & Hartley 2007; Zeng & Gu 2011). Also, for systems involving multiple deforming or moving volumetric bodies, methods such as the large deformation diffeomorphic metric mapping (Beg *et al.* 2005; Cao *et al.* 2005; Vercauteren *et al.* 2007) can be employed to optimally equip the domain with a differential background transport equation and enable the use of modal analysis to multibody systems.

## 3. Illustrative examples

Three examples of an undulating fish, a shape-changing ellipsoid and an airfoil with an active deflecting flap are selected to showcase the capabilities of the geometrically weighted modal analysis technique in dissecting the flow and forming a reduced-order representation of the flow.

### 3.1. *Undulating fish*

A fish model with undulatory motion is selected here to demonstrate the effectiveness of applying the geometrically weighted modal analysis to a deforming geometry. Using undulation as their primary propulsion method, fishes can swim with unparalleled maneuverability and efficiency compared with underwater vehicles. The famous experiment of the carcass of a rainbow trout passively undulating upstream (Beal *et al.* 2006) shows how important the interaction between the body deformation and surrounding flow field is. To learn from the aquatic animals, observations (Gray 1933; Blake 1983; Sfakiotakis, Lane & Davies 1999; Videler 2012) and metabolic rate measurements (Webb 1971; Clarke & Johnston 1999; Gillooly *et al.* 2001) are made, and different models have been proposed to explain the mechanics of fish swimming (Gero *et al.* 1952; Lighthill 1960; Wu 1971). These observations and models have been used to design and
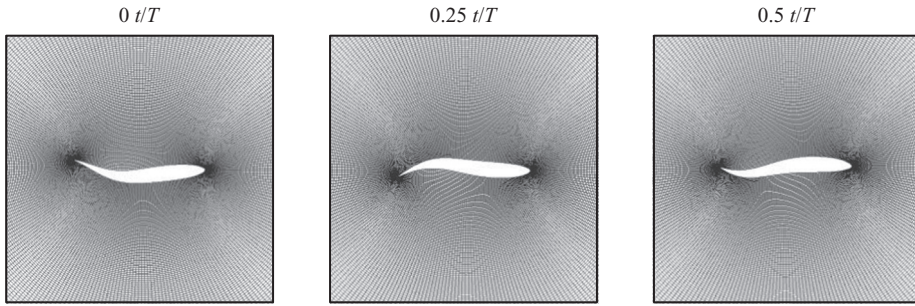
Figure 5. Snapshots of the deforming grid around the undulating fish model. Here $T$ represents the normalized period of the deformation.

build several fish robots and undulatory propellers (Triantafyllou & Triantafyllou 1995; Yu *et al.* 2004; Liu & Hu 2010; Marchese, Onal & Rus 2014). Computational fluid dynamics methods have been utilized to study fish locomotion. Techniques such as the vortex particle method (Ojima & Kamemoto 2005; Eldredge & Pisani 2008; Shoele & Zhu 2015), Euler–Lagrangian method (Kern & Koumoutsakos 2006) and immersed boundary method (Bozkurttas *et al.* 2006; Borazjani & Sotiropoulos 2008; Tytell *et al.* 2010; Maertens, Gao & Triantafyllou 2017) allow more delicate studies of fish swimming due to their capabilities to obtain high resolution full-field flow data. However, the methods either employ a deforming grid or require grid interpolation at the body contour, and this prevents the classical data-driven modal analysis tools from being employed to investigate the full flow field. Geometrically weighted modal decomposition solves this problem by transforming the undulating fish into a fixed cylinder with a time-invariant grid attached.

The fish model examined here is chosen to be a modified NACA0012 airfoil. The camber of the NACA0012 airfoil undergoes a lateral oscillation in the form of a streamwise downward travelling wave, described by

$$y_0 = A_m(x) \cos [2\pi(x + c\,t)], \quad 0 \le x \le 1, \tag{3.1}$$

where $A_m$ is the amplitude normalized with the fish length and $c$ is the phase speed of the travelling wave relative to the free stream velocity. From the experimental data of a steadily swimming saithe (Videler & Hess 1984), the backbone undulation motion of a fish can be approximated by a quadratic polynomial

$$A_m(x) = C_0 + C_1 x + C_2 x^2, \tag{3.2}$$

where the coefficients $C_0$, $C_1$ and $C_2$ are obtained from the recorded kinematic data, which gives $A_m(0) = 0.02$, $A_m(0.2) = 0.01$ and $A_m(1) = 0.1$. This profile is also used in many other types of research like Dong & Lu (2007) and Borazjani & Sotiropoulos (2008). The undulation motion is imposed as a pure lateral motion (Wassersug & von Sechendorf Hoff 1985; Liu *et al.* 1996). Three snapshots of the fish geometry are shown in figure 5. In this section we are going to show two cases with the same phase speed $c = 4$ but different Reynolds number $Re = U_\infty L/\nu = 1000, 4000$. We will focus on the near-body flow field to examine the performance of the GW-MD technique in capturing the near-body flow features.

The snapshots of the vorticity field behind the fish are shown in figure 6. From the time history and power spectrum of the lift coefficient plotted in figure 7, it is found that for both Reynolds numbers, the fish experiences periodic forcing at frequency $St = 0.25$, defined based on the free stream velocity and chord length. However, in the higher Reynolds
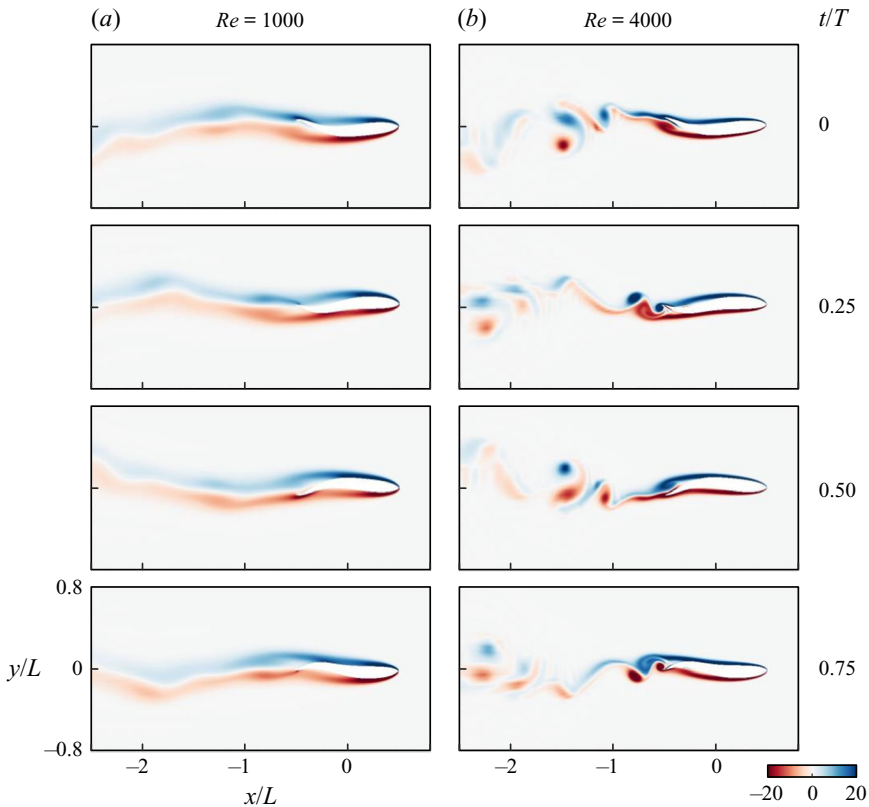
Figure 6. Snapshots of the undulating fish cases with the phase speed $c = 4$ and different Reynolds numbers $Re = 1000, 4000$. Here $T$ is the period of the motion. The colours represents the vorticity range.

number the vortices break down closer to the body and form multiple clusters. For all the following examples, the number of snapshots used in the modal analysis process covers at least 30 structural motion cycles with at least 10 snapshots per cycle. Figure 8 shows the GW-POD modes for the $Re = 1000$ case. The first column is obtained by directly applying the snapshot POD procedure to the vorticity in the transformed domain. For the second column, we premultiplied the vorticity with $\sqrt{|J|}$ to mitigate the transformation effect and denoted this as the physical-domain vorticity. The third and fourth columns show the horizontal and vertical velocities of GW-POD modes acquired in the transformed domain. As explained in the previous section, the Jacobian, in this case, has a greater determinant value at the trailing edge and the parts of the body with a large curvature. To help understand where the energy aggravates around the deforming body, we place the acquired modes on the grid constructed around the mean geometry. Note that the velocity modes are residing on the time-invariant grid in the transformed space, and mapping them to the mean grid is a visualization procedure.

It is found that less than six modes are required to capture over 95 % of the energy or enstrophy, regardless of which variable is selected to perform the GW-POD. The difference between using the vorticity or physical-domain vorticity is that the physical-domain modes have more emphasis on the leading edge region. Figure 9 shows the same modes with the inclusion of a wider downstream region. The reconstruction is still very efficient as only six leading modes recover 95 % of the energy content. We can observe that the
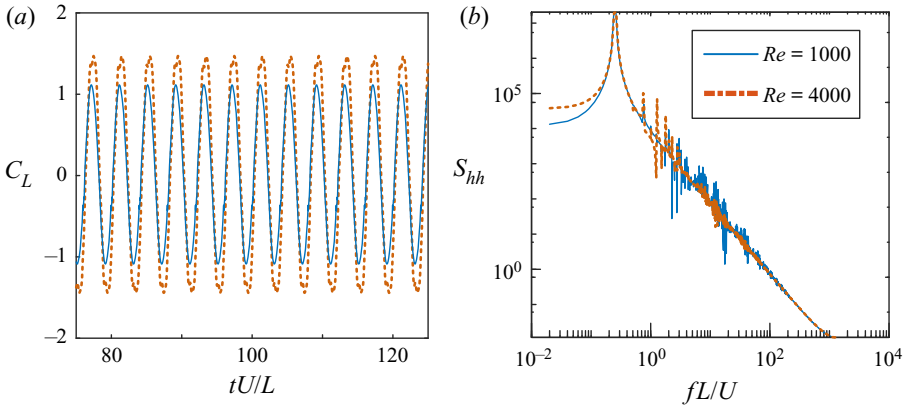
**911** A41-18

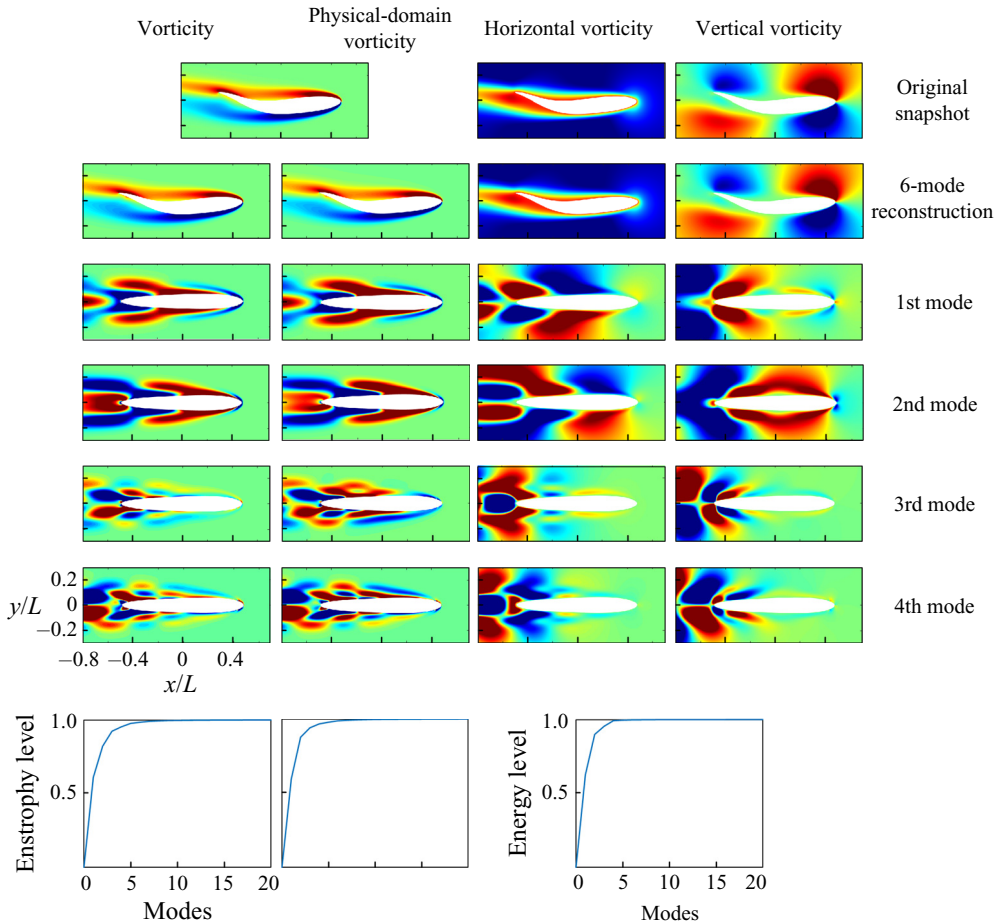Figure 7. (*a*) Time history and (*b*) power spectrum of the lift coefficient of the undulating fish model.



Figure 8. Geometrically weighted proper orthogonal decomposition modes, reconstruction of the snapshot and accumulated energy (enstrophy) level of the near-body flow field with the phase speed $c = 1$ and $Re = 1000$. To avoid cluttering the duplicate figure axis labels are not shown.
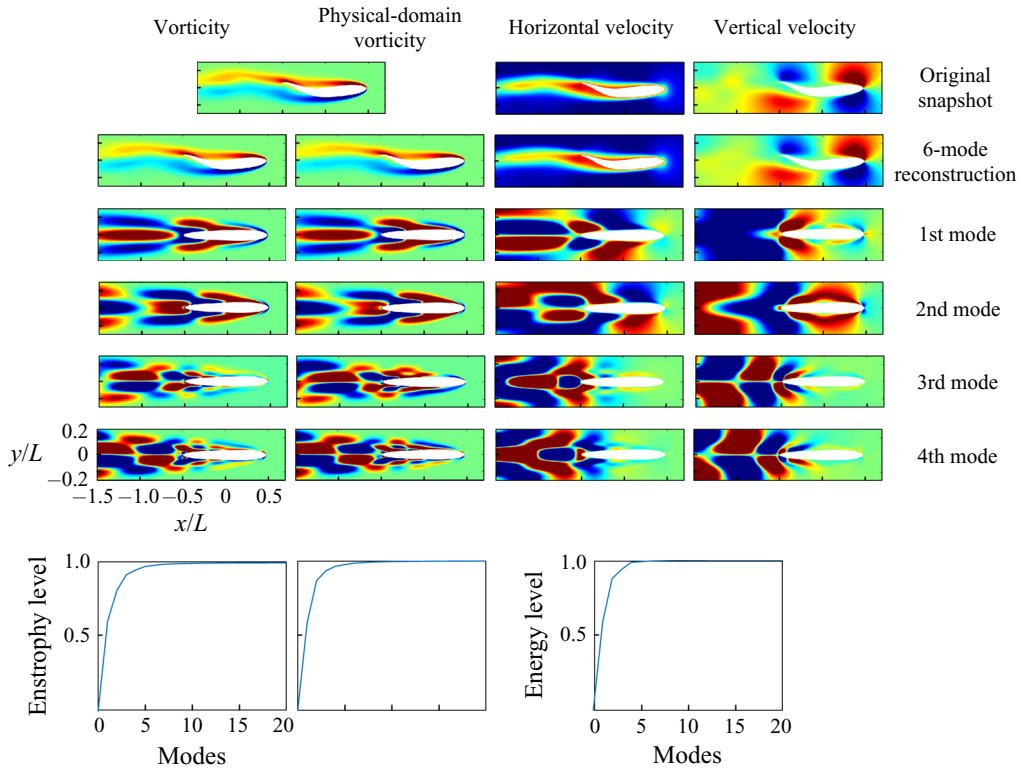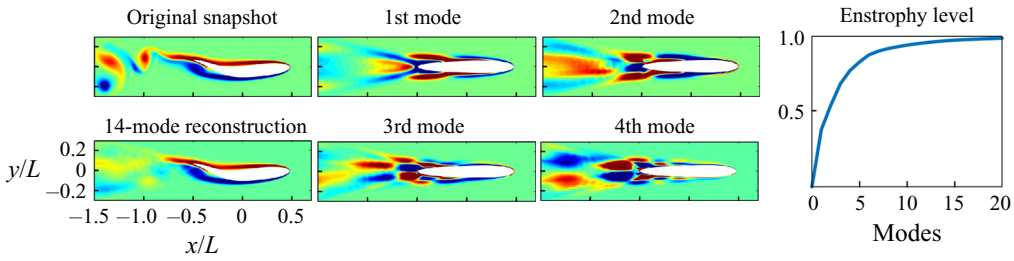
Figure 9. Geometrically weighted proper orthogonal decomposition modes, reconstruction of the snapshot and accumulated energy (enstrophy) level of the further downstream region flow field with the phase speed $c = 1$ and $Re = 1000$.

vorticity modes capture more details in the wake than the physical-domain vorticity modes. Both the vorticity and velocity modes display that most of the energy is accumulated around the mid-section and the trailing edge, where the primary vortex shedding happens. We can also observe that there are three sections with alternative vorticity along the body due to the sinusoidal wave shape. Since all three analyses using different variables have similar results, we will only report the modal analysis using the unmodified vorticity variable in the rest of the paper.

Now we look at the higher Reynolds number case. This case also includes a periodic flow, but instead of the more continuous wake observed in the $Re = 1000$ case, the wake consists of alternative vortices. The GW-POD modes are shown in figure 10 and it is noticed that the higher Reynolds number affects the dominant modes of the flow in two significant ways: the lack of coherent structures at further downstream locations and the need for more modes to reconstruct the flow field. The vortices shed from the trailing edge are propagating downstream as a vortex street, and more harmonic mode shapes are required to capture these coherent structures correctly. As a result, with only six modes, the reconstruction can hardly recover any wake distribution. Even with 14 modes, which contain just over 95 % of the enstrophy disturbance, the downstream region is still not represented well (figure 11). However, vorticity distribution in the near-body region does not change much with the inclusion of higher modes. One should anticipate that since the force experienced by the body is mostly affected by the near-body vortex distribution, the

Figure 10. Geometrically weighted proper orthogonal decomposition modes, reconstruction of the snapshot and accumulated energy (enstrophy) level of the vorticity field in the further downstream region with the phase speed $c = 1$ and $Re = 4000$.
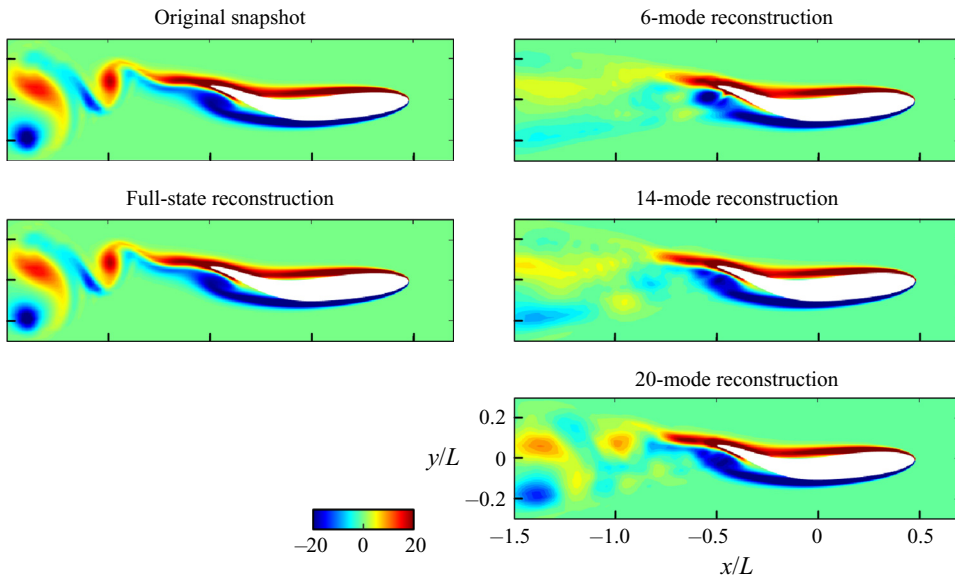


Figure 11. Reconstruction of the vorticity field with different numbers of modes for the case with phase speed $c = 1$ and larger Reynolds number $Re = 4000$.

hydrodynamic force acting on the body can be recovered with fewer modes than otherwise needed to reconstruct the whole flow field.

The undulating fish model shows how conformal mapping enables the modal analysis to be employed to study the flow field around a deforming body. The modes extracted with different variables have different indications of the dynamics but have similar reconstruction performance. Through two illustrative cases, we observe that the GW-POD modes can identify where the energy aggregates and reveal that the near-body vorticity distributions are similar in the dominant modes. Hence, we can explain why the force profiles are alike despite the very different wake. In the next section we will show how the geometrically weighted dynamic mode decomposition (GW-DMD) modes can be used to isolate system dynamics with characteristic frequencies.

### 3.2. Shape-changing ellipsoid

Deforming bodies in the flow stream have many engineering and biological applications such as icing plane wings (Bragg, Gregorek & Lee 1986) or dissolving icebergs (Taylor 1953; Eames 2008; Weymouth & Triantafyllou 2012), insect flight and ocean animals
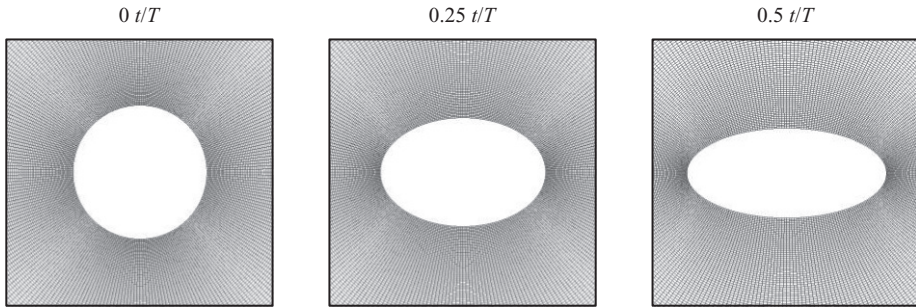
Figure 12. An ellipsoid expanding and contracting in the *X*-direction. Here *T* represents the normalized period of the deformation.

swimming by sudden shape change (Childress, Vandenberghe & Zhang 2006; Steele, Weymouth & Triantafyllou 2017). In this section we consider a canonical case of a deforming ellipsoid. As said in the previous section, we will use the vorticity in the transformed domain as the analysis object as it better captures the near-body flow field.

The geometry inspected here follows the work of Spagnolie & Shelley (2009). The semi-major axis $a(t)$ and semi-minor axis $b(t)$ of the body are changing with time, while the area of the ellipse $\pi a(t)b(t)$ is kept constant. The periodic deformation of the body is defined by

$$a(t) = \frac{1}{4}[5 + \sin(2\pi t)] \quad \text{and} \quad b(t) = \frac{1}{a(t)}. \quad (3.3a,b)$$

Several snapshots of the ellipsoid deformation and the corresponding body-fitted grid are shown in figure 12. The ambient flow velocity $U_\infty$ is used as the velocity scale, and the characteristic length is related to the area and defined as $L = \sqrt{a(t)b(t)}$. Here the Reynolds number is fixed at $Re = U_\infty L/\nu = 1000$.

In this section we focus on the effect of different deforming frequencies and the principal stretching direction on the flow around the body. We will use the pair (elongation direction, Strouhal number $St = f L/U_\infty$) to represent different cases. Figure 13 displays snapshots of the vorticity field of two cases, $(X, 1/2)$ and $(X, 1/8)$. While it is very challenging to understand the impact of the deformation on the flow from the snapshots alone, GW-DMD can be applied to the transformed cylindrical domain to investigate the modal frequency content of the flow field. Here, for brevity, only the real part of each GW-DMD mode is shown as similar observations can be made for the imaginary part.

The frequency-magnitude plots of the principal eigenvalue of GW-DMD modes for both cases are shown in figure 14. It is observed that for the $(X, 1/2)$ case, the harmonics of $St = 0.5$ (the frequency of the geometry deformation) have large peaks in magnitude; whereas such peaks are not present in the $(X, 1/8)$ case and the first three most significant peaks are at $St = 0.1916, 0.0045, 0$. The comparison of the spatial GW-DMD modes in the transformed domain, as shown in figure 15, reveals the difference between the two cases. The modes of the $(X, 1/2)$ case have a periodic wake with distinct alternative vortices shedding within a narrow region right behind the trailing end. The dominant modes have the inherent frequencies of the harmonics of the geometry change. On the other hand, the $(X, 1/8)$ case does not possess coherent spatial modes and instead the vortices distribute throughout the whole domain, forming a broad wake behind the body. These modes have frequencies that are not directly connected to body motion.

We can now see how body motion impacts the flow field from the snapshots shown in figure 13. In the $(X, 1/2)$ case the ellipsoid expands and contracts at a relatively fast
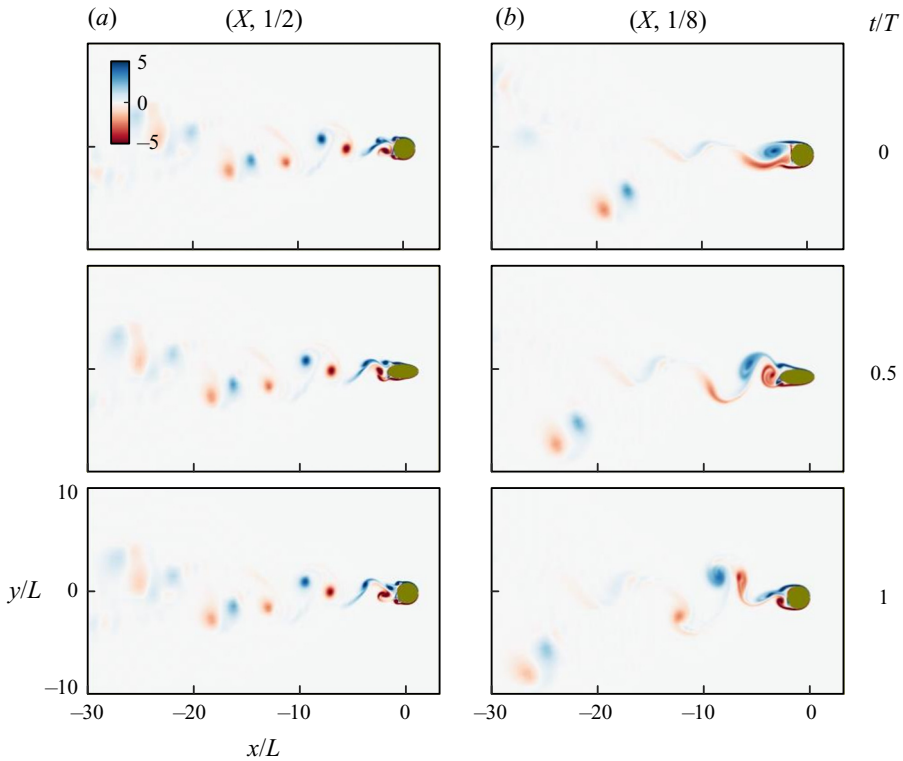
Figure 13. Snapshots of the vorticity field of the deforming ellipsoid for (*a*) (*X*, 1/2) and (*b*) (*X*, 1/8) over one structural motion period.
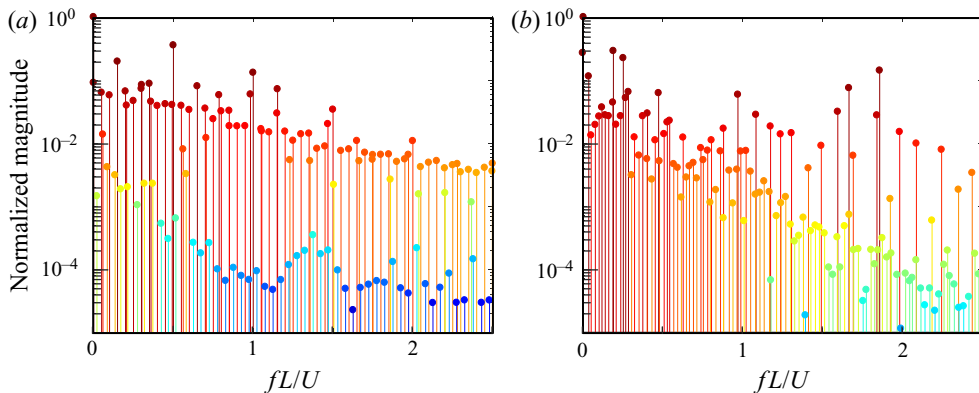


Figure 14. Frequency-magnitude plot of the GW-DMD modes of the case (*a*) (*X*, 1/2), (*b*) (*X*, 1/8).

rate compared with the vortex shedding time scale, and each time it elongates the vortices convect only a small distance downstream. However, before the vortices can completely separate away from the body, the ellipsoid body contracts and causes a reverse flow. This, in return, stops the shedding and forms a chain of smaller vortices near the surface. The pressure gradient formed by the vortex chain eventually affects the breakup of the shear
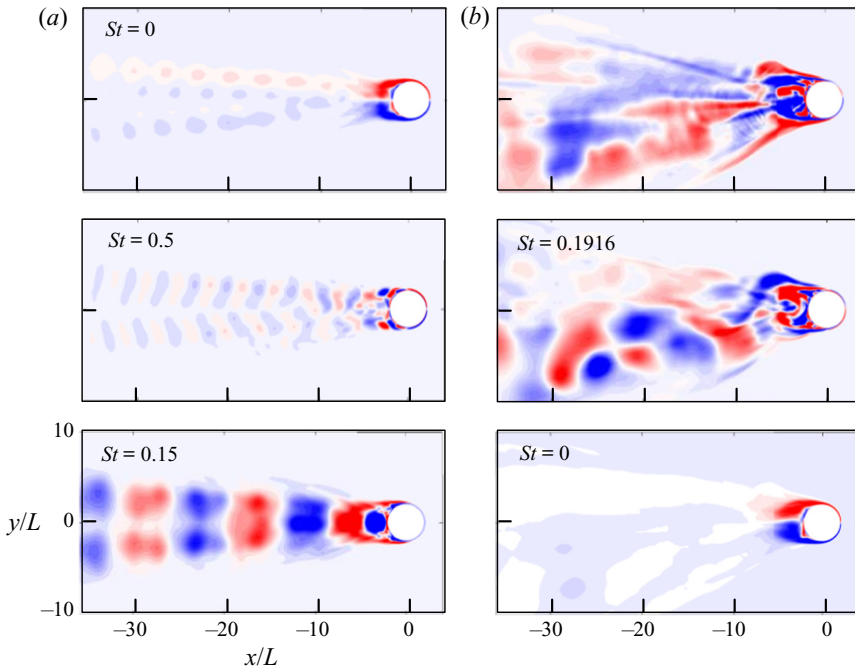
**911** A41-23

Figure 15. The first three GW-DMD vorticity mode pairs of the case (*a*) $(X, 1/2)$ and (*b*) $(X, 1/8)$ are shown from top to bottom in order.

layer and results in a wake that resembles the von-Karman vortex street. Hence, the vortex shedding frequency is controlled by the frequency of the shape changing.

Conversely, the $(X, 1/8)$ case shows a weak correlation between the vortex shedding and deformation. The reason is that the deformation occurs much slower compared with the previous case where strong reverse flow and suppression of the boundary layer separation are present. Here the vortices are formed based on the instantaneous geometry, and as a result, the chaotic behaviours with unsteady vortex shedding frequencies emerge.

Now we turn our focus to how the elongation direction affects the flow field. In figure 16 snapshots of the case $(Y, 1/2)$ are shown wherein the vortices appear in a broader area in the wake and do not follow any pattern. This observation can be explained by the presence of a powerful reverse flow from the large elongation in the cross-flow direction. Here the reverse flow with a large pressure gradient is so strong that the vortex shedding becomes unstable, quite different from the $(X, 1/2)$ case where the reverse flow is weak and the separated vortices are close to the body. To further investigate this observation, we compare the GW-POD representations of both $(X, 1/2)$ and $(Y, 1/2)$ cases. In figure 17 we see a distinctive difference in the accumulative normalized energy level. In the $(X, 1/2)$ case more than 90 % of its energy is in the first seven modes while the $(Y, 1/2)$ case requires 18 modes to reach the same level. This comparison shows the lack of coherent structures in the $(Y, 1/2)$ case and can be further supported by the spatial modes shown in figure 18. Compared with the alternative vortex pairs found in the leading GW-POD modes of the $(X, 1/2)$ case, the most energetic modes of the $(Y, 1/2)$ case exhibit a broad wake. In this case, the energy aggregates closer to the body due to the sparse wake and the near-body reverse flow.

For a periodic system, it can be useful to reconstruct the flow fields with truncated modes. This eliminates the less energetic modes often contaminated with noise and
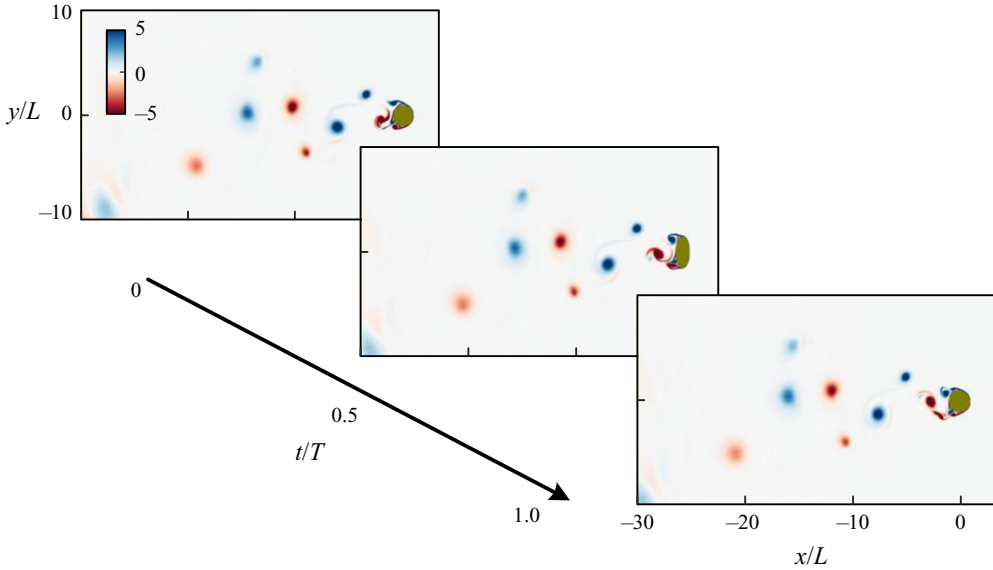
**911** A41-24

Figure 16. Snapshots of the vorticity field of deforming ellipsoid case $(Y, 1/2)$ over one structural motion period.

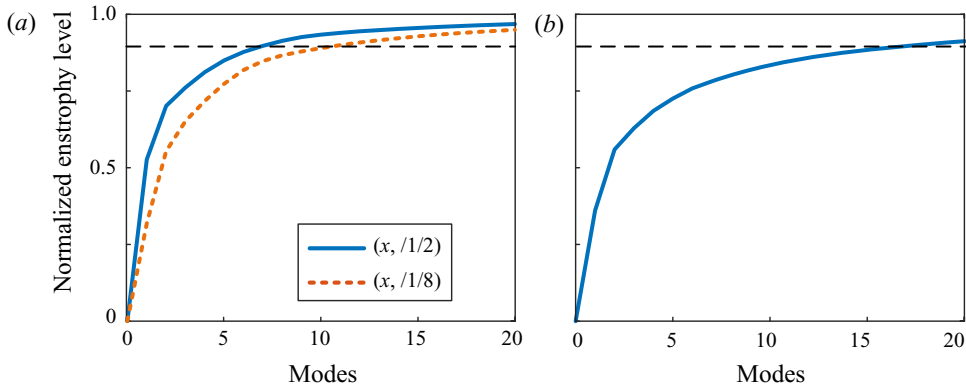

Figure 17. Normalized accumulative energy level of GW-POD vorticity modes for cases (*a*) $(X, 1/2)$ and $(X, 1/8)$, (*b*) $(Y, 1/2)$. The dashed line denotes the 90 % accumulated enstrophy level.

numerical errors and permits representing the system with less complexity. Figure 19 shows instantaneous snapshots for the $(X, 1/2)$ and $(Y, 1/2)$ cases and their reconstruction with a different number of GW-POD modes. It can be seen that with only eight modes, the reconstruction can capture most of the vorticity distribution in the $(X, 1/2)$ case, while in the $(Y, 1/2)$ case even with 20 modes, the reconstruction is not able to represent the flow field well. Furthermore, by using the geometrically weighted technique, the near-body dynamically critical flow features are given higher weights and the near-body flow field is captured with the first dominant modes while the higher modes essentially correct the vortices far from the ellipse.

In this section we used three cases of the shape-changing ellipsoid problem to demonstrate how the GW-MD can reveal the crucial dynamics of a system involving flow and deforming geometry. The characteristic frequencies acquired from GW-DMD
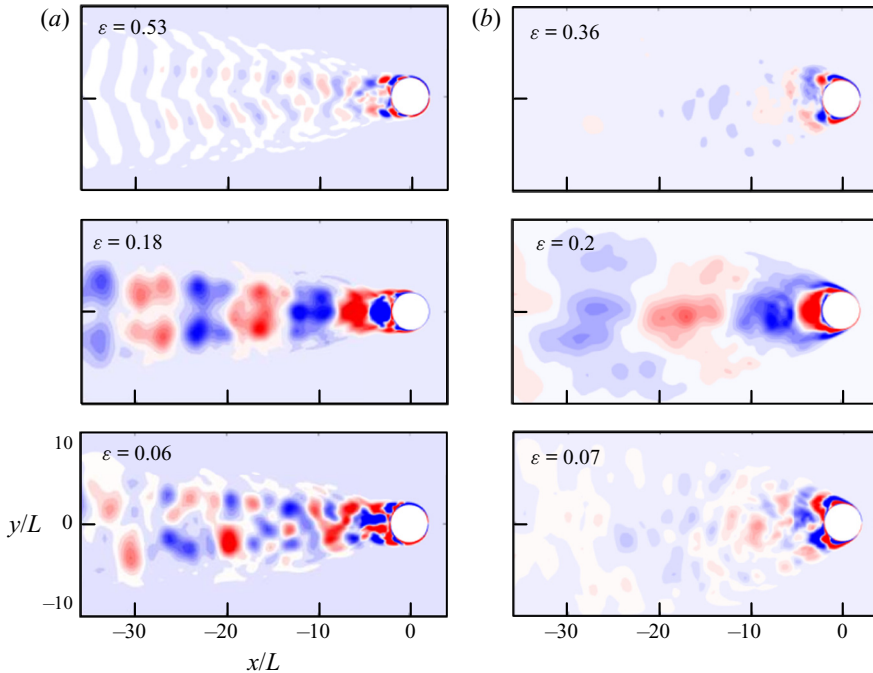
Figure 18. The first three most energetic GW-POD vorticity modes of the cases (*a*) (*X*, 1/2) and (*b*) (*Y*, 1/2) shown from top to bottom. The normalized energy level $\epsilon = \lambda_i / \sum_i \lambda_i$ of each mode is overlaid.

successfully separate the effect of the deformation versus the spatial fluid modes. The results show that the computed GW-POD modes are a good candidate to form a reduced-order representation of the flow field.

### 3.3. *Oscillating airfoil with an active deflecting flap*

Oscillating airfoils appear in diverse systems, such as the flutter of the aircraft wings (Kehoe 1995), animal locomotion (Guglielmini & Blondeaux 2004) or renewable energy extraction devices (Zhu & Peng 2009). To achieve better control of the oscillation of the airfoil, NASA and Boeing collaborated to develop the EET high-lift airfoil (Morgan 2002). The airfoil is equipped with actuators that can extend and deform the airfoil contours. We adopt this system as an example and focus on applying the GW-MD technique to inspect how the active deformation of the flap affects the flow structure in the wake. This system involves the feedback from the fluid loading force to the solid motion and exhibits a wide range of motion.

Figure 20 shows the physical model of an EET high-lift airfoil with the active trailing-edge flap. The physical parameters of the system include the geometric angle of attack $\alpha$ of the airfoil relative to the horizontal direction, the heaving displacement $h$ and the angle of the flap relative to the mean chord of the foil $\theta$. The aeroelastic oscillating effect is modelled by a set of linear and torsional spring-damper systems with damping and stiffness coefficients of $c_{h/\alpha}$ and $k_{h/\alpha}$, respectively.

The comprehensive study of the dynamics of this system was discussed more in-depth in Wang & Shoele (2018), and here the main focus instead is on the use of modal analysis to differentiate the flow structures between different cases.
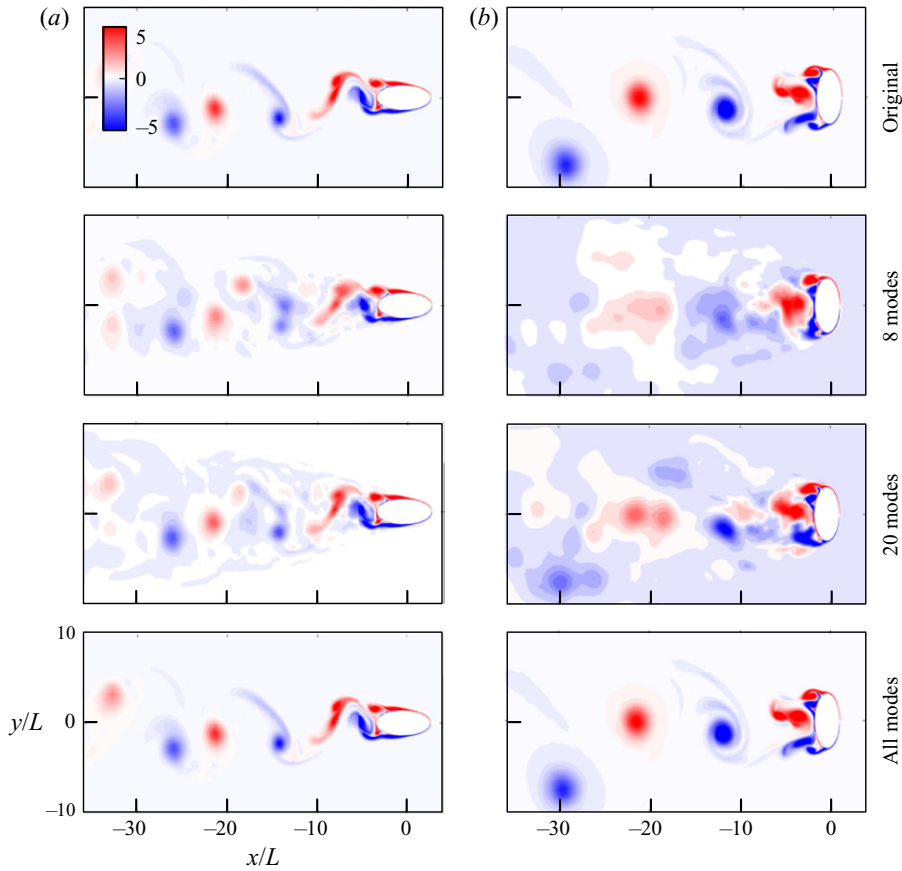
Figure 19. Reconstruction of the vorticity field of cases (*a*) (*X*, 1/2) and (*b*) (*Y*, 1/2) with different numbers of GW-POD modes. The top row shows the original snapshot.
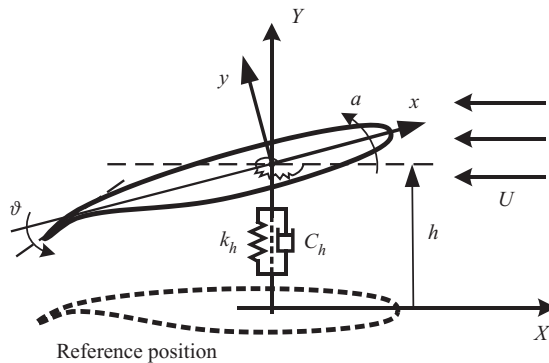


Figure 20. The physical model of an EET high-lift airfoil.

The foil is fixed at an angle of attack $\alpha$ and a sinusoidal oscillation is imposed on the flap to study how the flap motion influences the airfoil movement. The flap angle is $\theta = \theta_0 + A\sin(\Omega t)$, where $\theta_0$ and $A$ are the mean angle and amplitude, respectively, and $f = \Omega/2\pi$ is defined as the frequency of the oscillation. The Reynolds number ($Re = U_\infty L/v$) based
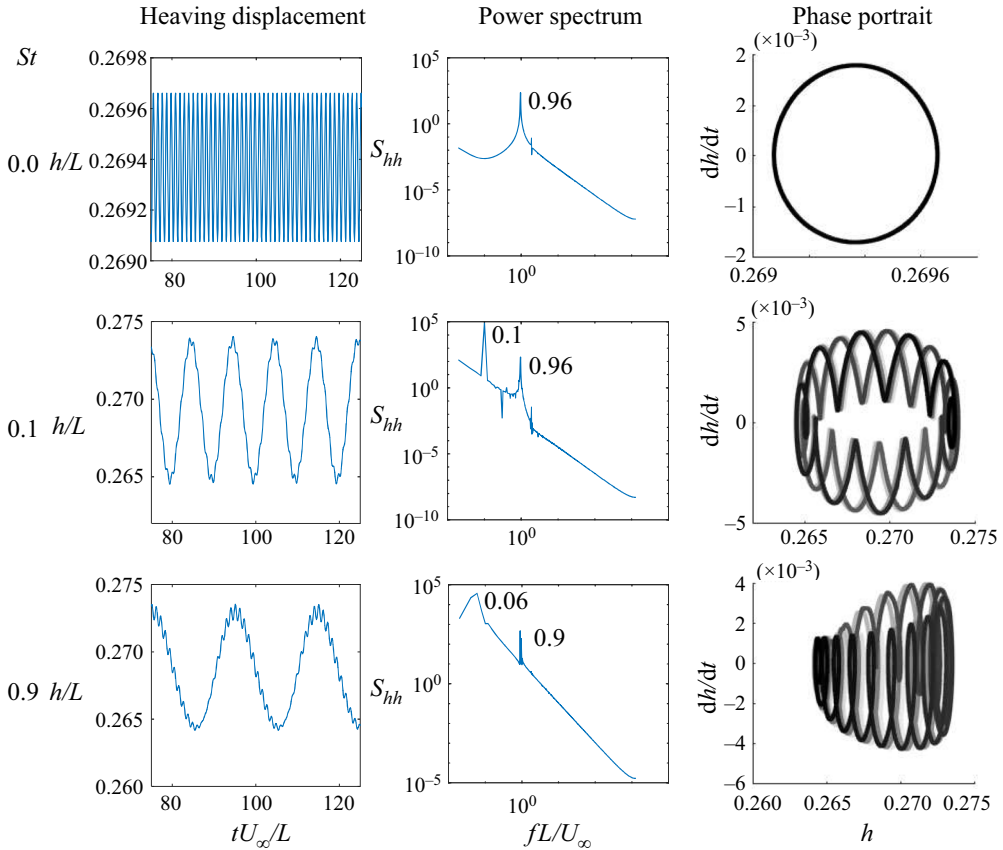
**911** A41-27

Figure 21. From left to right are time histories of heaving displacement, power spectrum and the phase portrait plot of cases $St = 0.0, 0.1, 0.9$ respectively shown from the top to bottom row.

on the chord length of the foil $L$ is chosen to be 1000. The flap length is $l = 0.12L$. In the rest of this section we use the Strouhal number, $St = fL/U_\infty$, to differentiate different cases while keeping other parameters fixed at $\alpha = 10°$, $A = 1.5°$ and $\theta_0 = 23.5°$.

Two cases with the flap frequency $St = 0.1$ and $0.9$, along with the control group with a stationary flap $St = 0$, are selected for this discussion. Figure 21 plots the heaving displacement time history of the airfoil and its power spectrum. The frequencies of the power peaks are denoted on the plot. We also provide the phase portrait plot, which is the mapping between the heaving displacement $h$ and velocity $dh/dt$, coloured from white to black in the temporal order.

From the control group, we observe a steady periodic vibration of the airfoil with frequency $St = 0.96$, as proved by the single-cycle phase portrait and a single dominant peak in the power spectrum. The heaving motion at the natural frequency is caused by the interaction between the alternative vortex shedding and the linear spring-damper system. When the actuation is activated, both the $St = 0.1$ and $St = 0.9$ cases exhibit a large heaving motion. The instantaneous snapshots within one actuation period for both cases are plotted in figure 22, which show a very similar wake profile and heaving amplitude between the two cases. It is possible to identify from the power spectrum and the torus-projected phase portrait that both cases are quasi-periodic systems with two distinct frequencies. However, the natural frequency $fL/U_\infty = 0.96$ is only present in the
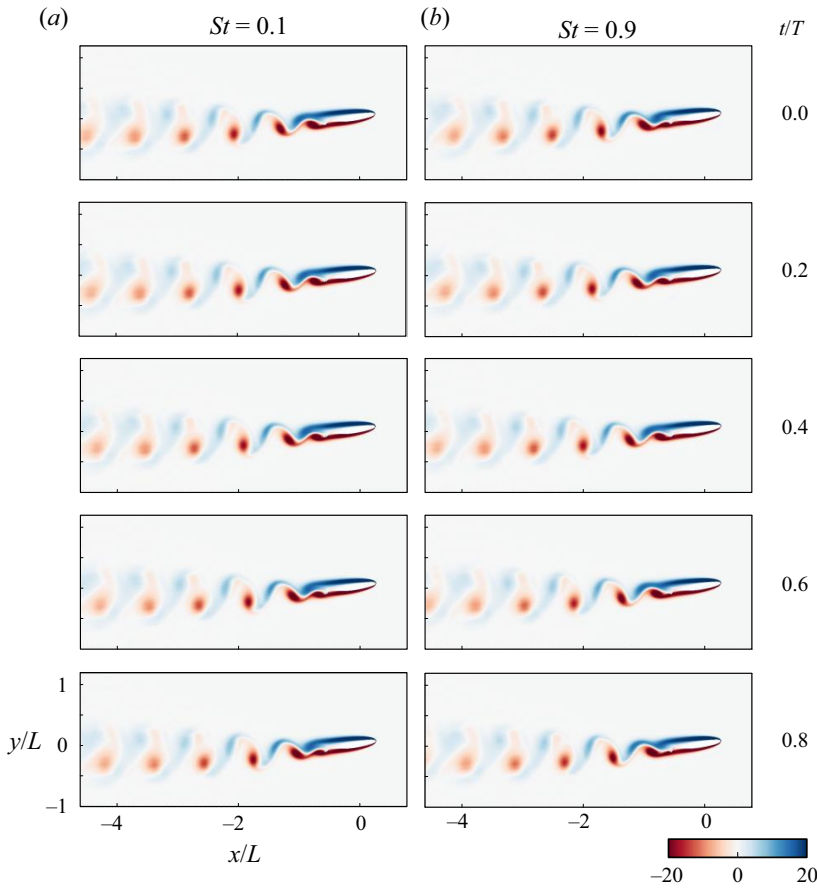
**911** A41-28

Figure 22. Instantaneous vorticity field of (*a*) $St = 0.1$ and (*b*) $St = 0.9$. The time span between each figure is normalized with the structural deformation period.

$St = 0.1$ case. Some questions arise from these observations: what role does the active flap play in creating these large-amplitude motions compared with the control case? What is the difference between the two actuated cases when their heaving time histories look similar? What flow features are connected to the dominant frequencies identified from the structural motion?

The GW-DMD modes can be utilized to answer the above questions. Figure 23(*a*) shows the principal eigenvalues (Ritz values) of the GW-DMD modes of the $St = 0.1$ case on the complex plane. The size of the points is scaled based on the magnitude of the corresponding modes, and the colour matches the frequency plot shown in figure 23(*b*). We should note that only the magnitudes with positive frequencies, i.e. Im$[\lambda] > 0$, are presented here. Most of the Ritz values are located on the unit circle $|\lambda| = 1$, which is expected as the system exhibits an orderly periodic vortex shedding. The four modes corresponding to the largest magnitudes are also plotted in figure 23(*c*). The one with the largest magnitude has a frequency of $St = 0$, representing the mean flow field. The second and the fourth modes have frequencies $St = 0.96$ and $St = 1.92$, respectively. They are related to the vortex-induced vibration natural frequencies. We will explain what mode 3 represents after looking at the GW-DMD modes of the case with the flapping frequency $St = 0.9$, shown in figure 24. In this case, most of the Ritz values still fall
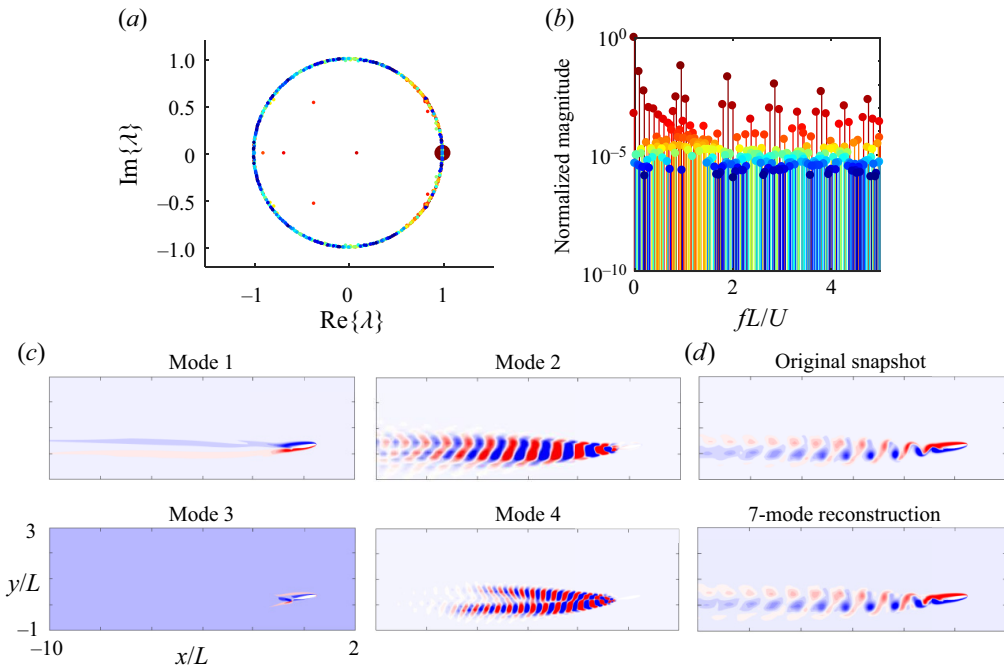
Figure 23. (*a*) The principal eigenvalues, (*b*) normalized magnitude relative to the frequency of GW-DMD modes, (*c*) first four modes with the largest magnitudes for case $St = 0.1$ with $\alpha = 10°$ and $A = 1.5°$, and (*d*) the comparison between the reconstructed and original vorticity field.

on the unit circle, indicating these modes do not grow or decay and are, therefore, either stationary or periodic. The first, second and fourth modes are identical to the $St = 0.1$ case, related to the mean and the natural frequency and its harmonics, respectively. However, the third mode is exceptionally different from the $St = 0.1$ case. In the $St = 0.9$ case, the third mode, with frequency $St = 0.9$, extends further downstream and signifies the vortex shedding caused by the rapid flap motion. When the flap moves downward, it induces large pressure gradient forces on a negative vortex layer on top of the flap. The flow separates but remains close to the upper surface of the trailing edge. When the flap moves upward, the vortex is propelled away. This creates an orderly wake that interacts with the geometry-induced vortex shedding wake structure in mode 2. The interference between these two modes creates the two peaks in the power spectrum at $St = 0.9$ and $St = 0.06$ (figure 21). The slight mismatch between the flap- and geometry-induced vortices results in the periodically large-amplitude heaving motion. On the other hand, with the flapping frequency of $St = 0.1$, the third mode only affects a small region close to the trailing edge. This implies that the slow-moving active flap, in this case, does not induce vortex shedding as the pressure gradient is much weaker. Instead, the movement of the flap modifies the geometry of the system and the departure angle of the geometry-induced wake, resulting in the large-amplitude motion with the same frequency as the flap motion $St = 0.1$.

The reconstruction of a selected frame with the first four mode pairs is shown in figures 23(*d*) and 24(*d*). The reconstruction is relatively accurate, meaning that the GW-DMD has successfully extracted the dominant dynamic features in both systems.

In this section we demonstrated the capability of GW-DMD modes for isolating important flow features along with their corresponding characteristic frequencies in an FSI system. Similar heaving responses from two cases with different flap frequencies are
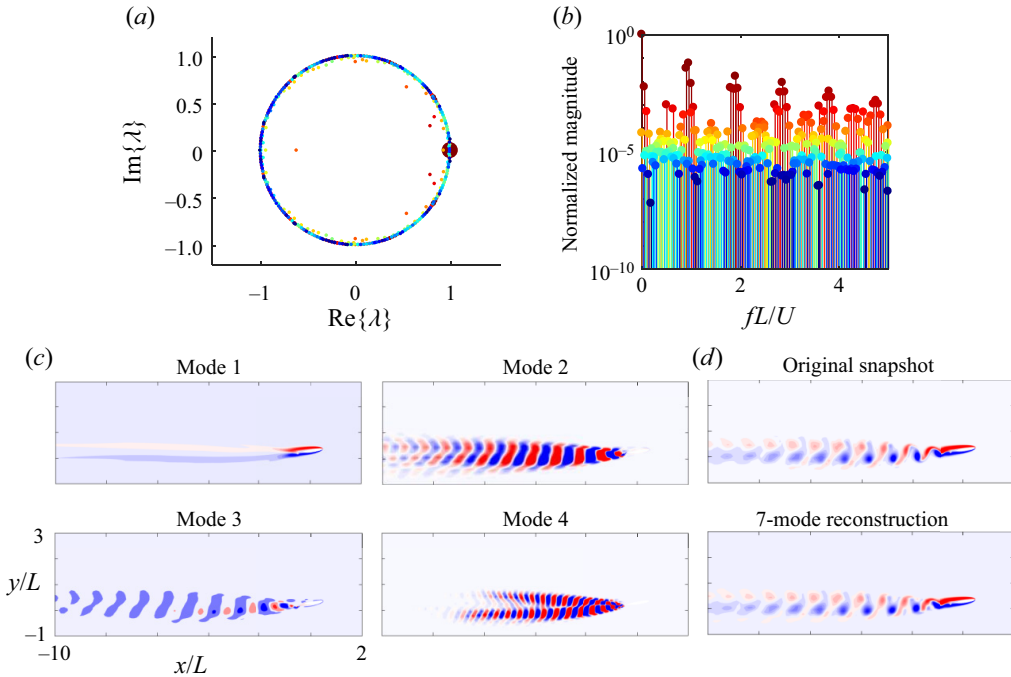
**911** A41-30

Figure 24. (*a*) The principal eigenvalues, (*b*) normalized magnitude relative to the frequency of GW-DMD modes, (*c*) first four modes with the largest magnitudes for case $St = 0.9$ with $\alpha = 10°$ and $A = 1.5°$, and (*d*) the comparison between the reconstructed and original vorticity field.

shown to have inherently different driving mechanisms using the GW-DMD modes. At low frequency, the flap does not induce vortex shedding but changes the direction of the wake. In contrast, at higher flap frequencies the fast structural deformation introduces new vortices to the wake and causes interference between this flap-induced and the geometry-induced wake leading to the periodic motion of the foil. This shows that the proposed method enables a discriminating modal analysis of FSI systems with a simultaneously moving and deforming body. The method can also be employed to extract information not directly available from the structural response or the wake dynamics.

## 4. Conclusions

In this paper a novel approach is proposed to systematically generate a spatial weighting based on local geometry to enable data-driven modal decomposition techniques for FSI problems involving a deforming and moving body. Through the conformal mapping process, we can map an arbitrary smooth geometry to a unit circle with the mapping incorporated in the Jacobian. We demonstrate how the GW-MD methods can successfully extract characteristic system dynamics with three illustrative examples. The GW-DMD modes can connect the frequency information obtained from the structural motion to flow structures. Besides, the GW-POD modes can be used to efficiently reconstruct the flow field and could serve as a basis for reduced-order modelling.

The GW-MD techniques have the benefits of being readily deployable to any smooth geometry. They can be post applied to experimental or numerical methods providing the geometry is available for the conformal mapping process. However, the method employed here is limited to two-dimensional analysis due to the constraint of much fewer

full conformal mappings available at higher dimensions. The current effort explores the possibility of extending the same concept to 3-D geometries using differential geometry techniques. In computational science research quasi-conformal mapping techniques have been used for shape recognition and surface mapping. Among different quasi-conformal techniques, there are methods such as discrete conformal mapping that preserves the angle of the mesh while being Laplacian conservative (Gotsman *et al.* 2003; Floater & Hormann 2005; Li & Hartley 2007), which is suitable for the current work. Also, harmonic mapping (Yanushauskas 1970; Wang *et al.* 2003) and volume parameterization of three-manifolds with small angular and volume distortions (Paillé & Poulin 2012; Kovalsky *et al.* 2015) are promising techniques to extend these analyses to higher dimensions. Advanced methods can also handle deformation in the structure (Zeng & Gu 2011; Lee, Lam & Lui 2016), which provides a path to extend the current study. With further development, the current method can be exploited to form ROMs and the subsequent design of control methods for shape-changing FSI problems. Another future direction is to relate interface forces between the solid and fluid to flow field modes using the force partitioning kernel technique (Martín-Alcántara, Fernandez-Feria & Sanmiguel-Rojas 2015; Zhang, Hedrick & Mittal 2015; Moriche, Flores & García-Villalba 2017; Wu, Liu & Liu 2018; Menon & Mittal 2020*b*) and essentially extend the modal analysis to solid using these force kernels. The conformal mapping provides a systematic way to investigate the fluid dynamic forces in a spatially fixed domain and retrieve a linear model describing how the structure interacts with the fluid.

The authors hope that the proposed framework opens up the path to systematically analyse FSI problems with deforming geometries and expand the horizon of analysing complex FSI systems.

**Declaration of interests.** The authors report no conflict of interest.

**Author ORCIDs.**
Kourosh Shoele https://orcid.org/0000-0003-2810-0065.

## Appendix A. Validation of the algorithm

To validate the numerical algorithm used in this study, we compare our predictions to literature for several benchmark canonical problems.

The first case is a stationary cylinder placed in uniform flow. The Reynolds number *Re* is based on the diameter of the cylinder, and the incoming flow speed ranges from 50 to 1000.

The computational grid is set up with the same mapping procedure introduced in § 2, with the resolution $400 \times 512$ in the radial and angular directions, respectively, and extended to 50 diameters of the cylinder. The time interval is chosen to be $\Delta t = 0.0005$. Figure 25 shows the flow field compared with results from Saiki & Biringen (1996) and Ding *et al.* (2007). The present model could correctly replicate the position and intensity of the coherent structure in both Reynolds numbers 100 and 200. The Strouhal number based on the lift, defined as $St = fD/U$ with $D$ as the diameter of the cylinder, is plotted in figure 26, and compared with the results obtained by other authors experimentally (Roshko 1961) and numerically (Lei, Cheng & Kavanagh 2000; Zhao *et al.* 2005). Present results agree well with the previously reported numerical results but slightly higher than the experimental results due to the 3-D effect.
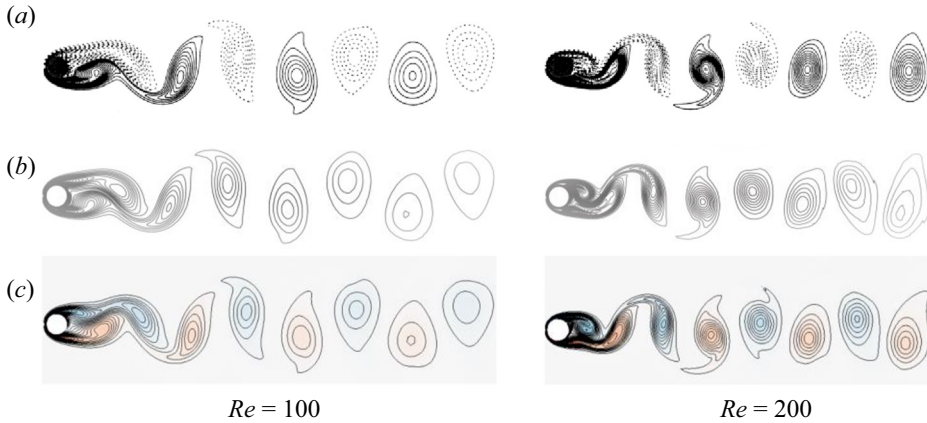
Figure 25. Vorticity field behind a cylinder predicted by (*a*) Saiki & Biringen (1996), (*b*) Ding *et al.* (2007) and (*c*) the current method.
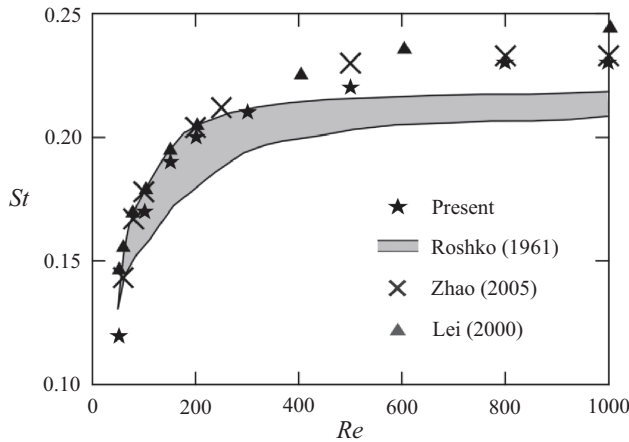


Figure 26. Strouhal number of the cylinder flow. The two lines indicate the range of experimental results from Roshko (1961).

The second case is the lift coefficient of a translating ellipsoid at different angles of attack. The canonical problem is compared with the results from Wang (2000) where, as shown in figure 27, a good match is found.

The third case is the dynamic force measurement comparison of a translating and rotating wing described by Wang, Birch & Dickinson (2004). The ratio of the translational motion amplitude and the chord length is $A_0/c = 2.8$, and there is no phase difference between the translational and rotational motion. The angle of attack is fixed at $\alpha_0 = \pi/2$, the amplitude of pitching angle at $\beta = \pi/4$ and the frequency at $f = 0.25$. The Reynolds number based on the translational amplitude $A_0$ and chord length $c$ is 75. Following the definition by Wang *et al.* (2004), the forces are normalized with the maximum quasi-steady forces. Figure 28 and table 1 show the comparison of the lift and drag coefficients between current work, both simulation and experimental results provided by Wang *et al.* (2004), and numerical results from Eldredge (2007). Due to the 3-D effect, none of the numerical results can perfectly replicate the force information acquired from
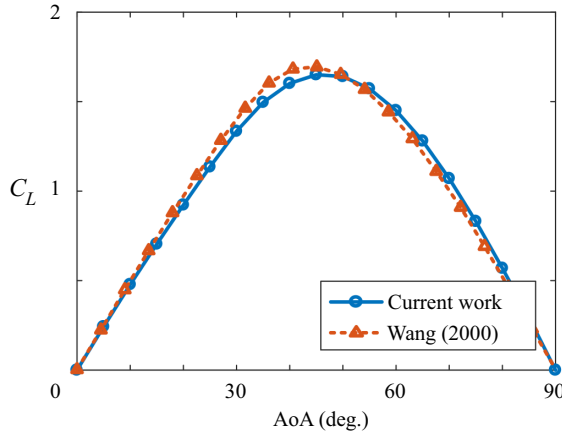
Figure 27. Comparison of the lift coefficient of an ellipsoid at different angles of attack with the literature.
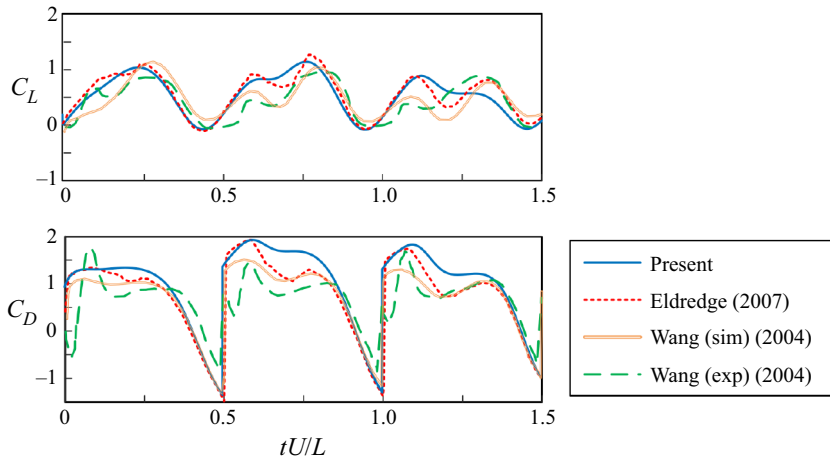


Figure 28. Dynamic force coefficients of a flapping elliptic wing.

the experiments. However, the maximum value and the overall profile are comparable between the numerical results and the proposed algorithm should be sufficient to support the current work.

## Appendix B. Formulation of the modified Navier–Stokes equation in the transformed domain

To solve the Navier–Stokes equation in the transformed space, we need to modify the Navier–Stokes equations accordingly. We follow the procedure introduced by Batchelor (2000) to achieve this. The transformation process has two stages: first, the global Cartesian coordinate $(x, y)$ is transformed into a moving reference frame $(X, Y)$ considering the heaving and pitching motion of the structure, then through the conformal mapping procedure $(X, Y)$ is transformed into a cylindrical coordinate system $r e^{i\phi}$.

A smooth geometry is considered in the Cartesian coordinate system $(x, y)$. The structure is assumed to have heaving and pitching motion, with the amplitude being $h$ and $\alpha$, respectively. The Navier–Stokes equations to be solved, represented in the

**911** A41-34

| $C_L$ | Max | Min | Avg. | r.m.s. |
|---|---|---|---|---|
| Wang (2004), exp. | 0.9971 | −0.1078 | 0.4440 | 0.5311 |
| Wang (2004), num. | 1.1459 | −0.1142 | 0.4902 | 0.5680 |
| Eldredge (2007) | 1.2663 | −0.1114 | 0.5984 | 0.6992 |
| Current method | 1.1392 | −0.0798 | 0.5282 | 0.6412 |

| $C_D$ | Max | Min | Avg. | r.m.s. |
|---|---|---|---|---|
| Wang (2004), exp. | 1.7791 | −0.8636 | 0.6052 | 0.8697 |
| Wang (2004), num. | 1.5334 | −1.3274 | 0.4075 | 0.8284 |
| Eldredge (2007) | 1.9298 | −1.4816 | 0.7041 | 1.1123 |
| Current method | 1.9311 | −1.3636 | 0.9705 | 1.2855 |

Table 1. Statistical comparison of the dynamic force coefficients of a flapping elliptic wing.

vorticity-stream function $(\omega - \psi)$ form, are

$$\frac{\partial \omega}{\partial t} + \frac{\partial \psi}{\partial y}\frac{\partial \omega}{\partial x} - \frac{\partial \psi}{\partial x}\frac{\partial \omega}{\partial y} = \frac{1}{Re}\left[\frac{\partial^2 \omega}{\partial x^2} + \frac{\partial^2 \omega}{\partial y^2}\right], \tag{B1}$$

$$\frac{\partial^2 \psi}{\partial x^2} + \frac{\partial^2 \psi}{\partial y^2} = -\omega. \tag{B2}$$

With the coordinate transformation

$$(X, Y) = x(\cos\alpha, -\sin\alpha) + (y - h)(\sin\alpha, \cos\alpha), \tag{B3}$$

we acquire the Navier–Stokes equation in the $(X, Y)$ domain as

$$\frac{\partial \omega}{\partial t} + U\frac{\partial \omega}{\partial X} + V\frac{\partial \omega}{\partial Y} = \frac{1}{Re}\left[\frac{\partial^2 \omega}{\partial X^2} + \frac{\partial^2 \omega}{\partial Y^2}\right], \tag{B4}$$

$$\frac{\partial^2 \psi}{\partial X^2} + \frac{\partial^2 \psi}{\partial Y^2} = -\omega, \tag{B5}$$

where $U$ and $V$ are

$$U = u\cos\alpha + \left(v - \frac{dh}{dt}\right)\sin\alpha + Y\frac{d\alpha}{dt}, \tag{B6}$$

$$V = \left(v - \frac{dh}{dt}\right)\cos\alpha - u\sin\alpha - X\frac{d\alpha}{dt}, \tag{B7}$$

while $u = \partial\psi/\partial y$ and $v = -\partial\psi/\partial x$ are the horizontal and vertical velocities under the $(x, y)$ coordinate.

Now we look at the transformation from the $(X, Y)$ plane to the $\zeta = (\xi, \eta)$ plane. We can assume that the transformation and inverse transformation are

$$\xi = f(X, Y), \quad \eta = g(X, Y), \tag{B8}$$

$$X = F(\xi, \eta), \quad Y = G(\xi, \eta). \tag{B9}$$

It follows that

$$\begin{bmatrix} dX \\ dY \end{bmatrix} = \begin{bmatrix} F_\xi & F_\eta \\ G_\xi & G_\eta \end{bmatrix}\begin{bmatrix} d\xi \\ d\eta \end{bmatrix}, \tag{B10}$$

and

$$\begin{bmatrix} d\xi \\ d\eta \end{bmatrix} = \frac{1}{F_\xi G_\eta - F_\eta G_\xi} \begin{bmatrix} G_\eta & -F_\eta \\ -G_\xi & F_\xi \end{bmatrix} \begin{bmatrix} dX \\ dY \end{bmatrix}, \tag{B11}$$

where the subscript variables denote derivation relative to the variable. We define the determinant of the Jacobian to be $|J| = F_\xi G_\eta - F_\eta G_\xi$. Then we can follow the relations given in Batchelor (2000) to calculate the convective term. We have the relation

$$(dX)^2 + (dY)^2 = (F_\xi^2 + G_\xi^2)(d\xi)^2 + (F_\eta^2 + G_\eta^2)(d\eta)^2 + 2(F_\xi F_\eta + G_\xi G_\eta)\, d\xi\, d\eta. \tag{B12}$$

Note that since the transformation is conformal, the Cauchy–Riemann relation holds and the last term goes to zero, i.e. $F_\xi F_\eta + G_\xi G_\eta = 0$, and, hence, the scaling factors are

$$h_1 = \sqrt{F_\xi^2 + G_\xi^2} = \sqrt{F_\xi G_\eta + G_\xi(-F_\eta)} = \sqrt{|J|}, \tag{B13}$$

$$h_2 = \sqrt{F_\eta^2 + G_\eta^2} = \sqrt{F_\eta(-G_\xi) + G_\eta F_\xi} = \sqrt{|J|}. \tag{B14}$$

The unit vectors parallel to the coordinate lines are

$$\tilde{a} = h_1 \left( \frac{\partial \xi}{\partial X}, \frac{\partial \xi}{\partial Y} \right) = \frac{1}{\sqrt{|J|}} \left( \frac{\partial Y}{\partial \eta}, -\frac{\partial X}{\partial \eta} \right), \tag{B15}$$

$$\tilde{b} = h_2 \left( \frac{\partial \eta}{\partial X}, \frac{\partial \eta}{\partial Y} \right) = \frac{1}{\sqrt{|J|}} \left( -\frac{\partial Y}{\partial \xi}, \frac{\partial X}{\partial \xi} \right). \tag{B16}$$

We then recover the convective term in the $(\xi, \eta)$ domain as

$$v \cdot \nabla \omega = (V_\xi, V_\eta) \cdot \left( \frac{\tilde{a}}{h_1} \frac{\partial}{\partial \xi}, \frac{\tilde{b}}{h_2} \frac{\partial}{\partial \eta} \right) \omega. \tag{B17}$$

The Navier–Stokes equations in the $(\xi, \eta)$ are thus

$$\frac{\partial \omega}{\partial t} + \frac{V_\xi}{\sqrt{|J|}} \frac{\partial \omega}{\partial \xi} + \frac{V_\eta}{\sqrt{|J|}} \frac{\partial \omega}{\partial \eta} = \frac{1}{Re\,|J|} \left[ \frac{\partial^2 \omega}{\partial \xi^2} + \frac{\partial^2 \omega}{\partial \eta^2} \right], \tag{B18}$$

$$\frac{\partial^2 \psi}{\partial \xi^2} + \frac{\partial^2 \psi}{\partial \eta^2} = -|J|\omega, \tag{B19}$$

with the $V_\xi$ and $V_\eta$ being

$$V_\xi = \frac{1}{\sqrt{|J|}} \left\{ (F_\eta G_t - F_t G_\eta) + \left[ \frac{\partial \psi}{\partial \eta} + \left( Y\frac{d\alpha}{dt} - \frac{dh}{dt}\sin\alpha \right) G_\eta \right. \right.$$
$$\left. \left. + \left( X\frac{d\alpha}{dt} + \frac{dh}{dt}\cos\alpha \right) F_\eta \right] \right\}, \tag{B20}$$

$$V_\eta = \frac{1}{\sqrt{|J|}} \left\{ (G_\xi F_t - G_t F_\xi) + \left[ -\frac{\partial \psi}{\partial \xi} - \left( Y\frac{d\alpha}{dt} - \frac{dh}{dt}\sin\alpha \right) G_\xi \right. \right.$$
$$\left. \left. - \left( X\frac{d\alpha}{dt} + \frac{dh}{dt}\cos\alpha \right) F_\xi \right] \right\}. \tag{B21}$$

Finally, we introduce the polar coordinate $(r, \theta)$ in the plane $(\xi, \eta)$. The final form of the Navier–Stokes equations in the $(r, \theta)$ are thus

$$\frac{\partial \omega}{\partial t} + \frac{1}{\sqrt{|J|}} \left[ V_r \frac{\partial \omega}{\partial r} + \frac{V_\theta}{r} \frac{\partial \omega}{\partial \theta} \right] = \frac{1}{Re\,|J|} \left[ \frac{\partial^2 \omega}{\partial r^2} + \frac{1}{r} \frac{\partial \omega}{\partial r} + \frac{1}{r^2} \frac{\partial^2 \omega}{\partial \theta^2} \right], \qquad (B22)$$

$$\frac{\partial^2 \psi}{\partial r^2} + \frac{1}{r} \frac{\partial \psi}{\partial r} + \frac{1}{r^2} \frac{\partial^2 \psi}{\partial \theta^2} = -|J|\omega, \qquad (B23)$$

with $V_r$ and $V_\theta$ being

$$V_r = V_\xi \cos \theta + V_\eta \sin \theta, \qquad (B24)$$

$$V_\theta = -V_\xi \sin \theta + V_\eta \cos \theta. \qquad (B25)$$

## REFERENCES

AFANASIEV, K. & HINZE, M. 2001 *Adaptive control of a wake flow using proper orthogonal decomposition.* In *Shape Optimization And Optimal Design* (ed. M.P. Polis, J. Cagnol & J.-P. Zolésio), chap. 13. CRC Press.

ANTTONEN, J.S.R., KING, P.I. & BERAN, P.S. 2003 POD-based reduced-order models with deforming grids. *Math. Comput. Model.* **38** (1–2), 41–62.

ASTRID, P., WEILAND, S., WILLCOX, K. & BACKX, T. 2008 Missing point estimation in models described by proper orthogonal decomposition. *IEEE Trans. Autom. Control* **53** (10), 2237–2251.

AUBRY, N., HOLMES, P., LUMLEY, J.L. & STONE, E. 1988 The dynamics of coherent structures in the wall region of a turbulent boundary layer. *J. Fluid Mech.* **192**, 115–173.

BATCHELOR, G.K. 2000 *An Introduction to Fluid Dynamics.* Cambridge Mathematical Library, Cambridge University Press.

BAZILEVS, Y., TAKIZAWA, K. & TEZDUYAR, T.E. 2013 Challenges and directions in computational fluid–structure interaction. *Math. Models Methods Appl. Sci.* **23** (02), 215–221.

BEAL, D.N., HOVER, F.S., TRIANTAFYLLOU, M.S., LIAO, J.C. & LAUDER, G.V. 2006 Passive propulsion in vortex wakes. *J. Fluid Mech.* **549**, 385–402.

BEG, M.F., MILLER, M.I., TROUVÉ, A. & YOUNES, L. 2005 Computing large deformation metric mappings via geodesic flows of diffeomorphisms. *Intl J. Comput. Vis.* **61** (2), 139–157.

BLAKE, R.W. 1983 *Fish Locomotion.* CUP Archive.

BLEVINS, R.D. 1977 *Flow-Induced Vibration.* Van Nostrand Reinhold Co.

BORAZJANI, I. & SOTIROPOULOS, F. 2008 Numerical investigation of the hydrodynamics of carangiform swimming in the transitional and inertial flow regimes. *J. Expl Biol.* **211** (10), 1541–1558.

BOZKURTTAS, M., DONG, H., MITTAL, R., MADDEN, P. & LAUDER, G. 2006 Hydrodynamic performance of deformable fish fins and flapping foils. In *44th AIAA Aerospace Sciences Meeting and Exhibit*, p. 1392. AIAA.

BOZKURTTAS, M., MITTAL, R., DONG, H., LAUDER, G.V. & MADDEN, P. 2009 Low-dimensional models and performance scaling of a highly deformable fish pectoral fin. *J. Fluid Mech.* **631**, 311–342.

BRAGG, M.B., GREGOREK, G.M. & LEE, J.D. 1986 Airfoil aerodynamics in icing conditions. *J. Aircraft* **23** (1), 76–81.

CAO, Y., MILLER, M.I., WINSLOW, R.L. & YOUNES, L. 2005 Large deformation diffeomorphic metric mapping of vector fields. *IEEE Trans. Med. Imaging* **24** (9), 1216–1230.

CESUR, A., CARLSSON, C., FEYMARK, A., FUCHS, L. & REVSTEDT, J. 2014 Analysis of the wake dynamics of stiff and flexible cantilever beams using POD and DMD. *Comput. Fluids* **101**, 27–41.

CHILDRESS, S., VANDENBERGHE, N. & ZHANG, J. 2006 Hovering of a passive body in an oscillating airflow. *Phys. Fluids* **18** (11), 117103.

CHRISTENSEN, E.A., BRØNS, M. & SØRENSEN, J.N. 1999 Evaluation of proper orthogonal decomposition–based decomposition techniques applied to parameter-dependent nonturbulent flows. *SIAM. J. Sci. Comput.* **21** (4), 1419–1434.

CLARKE, A. & JOHNSTON, N.M. 1999 Scaling of metabolic rate with body mass and temperature in teleost fish. *J. Animal Ecol.* **68** (5), 893–905.

CONNELL, B.S.H. & YUE, D.K.P. 2007 Flapping dynamics of a flag in a uniform stream. *J. Fluid Mech.* **581**, 33–67.

DING, H., SHU, C., YEO, K.S. & XU, D. 2007 Numerical simulation of flows around two circular cylinders by mesh-free least square-based finite difference methods. *Intl J. Numer. Meth. Fluids* **53** (2), 305–332.

DONG, G.-J. & LU, X.-Y. 2007 Characteristics of flow over traveling wavy foils in a side-by-side arrangement. *Phys. Fluids* **19** (5), 057107.

EAMES, I. 2008 Rapidly dissolving dense bodies in an inviscid fluid. *Proc. R. Soc.* A **464** (2099), 2985–3002.

ELDREDGE, J.D. 2007 Numerical simulation of the fluid dynamics of 2D rigid body motion with the vortex particle method. *J. Comput. Phys.* **221** (2), 626–648.

ELDREDGE, J.D. 2019 *Mathematical Modeling of Unsteady Inviscid Flows*. Springer.

ELDREDGE, J.D. & PISANI, D. 2008 Passive locomotion of a simple articulated fish-like system in the wake of an obstacle. *J. Fluid Mech.* **607**, 279–288.

FLANDERS, H. 1966 Liouville's theorem on conformal mapping. *J. Maths Mech.* **15** (1), 157–161.

FLOATER, M.S. & HORMANN, K. 2005 Surface parameterization: a tutorial and survey. In *Advances in Multiresolution for Geometric Modelling* (ed. N.A. Dodgson, M.S. Floater & M.A. Sabin), pp. 157–186. Springer.

FOGLEMAN, M., LUMLEY, J., REMPFER, D. & HAWORTH, D. 2004 Application of the proper orthogonal decomposition to datasets of internal combustion engine flows. *J. Turbul.* **5** (23), 1–3.

FRENO, B.A & CIZMAS, P.G.A. 2014 A proper orthogonal decomposition method for nonlinear flows with deforming meshes. *Intl J. Heat Fluid Flow* **50**, 145–159.

GERO, D.R., *et al.* 1952 The hydrodynamic aspects of fish propulsion. American Museum Novitates; no. 1601.

GILLOOLY, J.F., BROWN, J.H., WEST, G.B., SAVAGE, V.M. & CHARNOV, E.L. 2001 Effects of size and temperature on metabolic rate. *Science* **293** (5538), 2248–2251.

GOTSMAN, C., GU, X. & SHEFFER, A. 2003 Fundamentals of spherical parameterization for 3D meshes. In *ACM Transactions on Graphics (TOG)*, vol. 22, pp. 358–363. ACM.

GOZA, A. & COLONIUS, T. 2018 Modal decomposition of fluid–structure interaction with application to flag flapping. *J. Fluids Struct.* **81**, 728–737.

GRAY, J. 1933 Studies in animal locomotion: I. The movement of fish with special reference to the EEL. *J. Expl Biol.* **10** (1), 88–104.

GU, X., WANG, Y., CHAN, T.F., THOMPSON, P.M. & YAU, S.-T. 2004 Genus zero surface conformal mapping and its application to brain surface mapping. *IEEE Trans. Med. Imaging* **23** (8), 949–958.

GUGLIELMINI, L. & BLONDEAUX, P. 2004 Propulsive efficiency of oscillating foils. *Eur. J. Mech. B/Fluids* **23** (2), 255–278.

HEMATI, M.S., WILLIAMS, M.O. & ROWLEY, C.W. 2014 Dynamic mode decomposition for large and streaming datasets. *Phys. Fluids* **26** (11), 111701.

HOLMES, P., LUMLEY, J.L., BERKOOZ, G. & ROWLEY, C.W. 2012 *Turbulence, Coherent Structures, Dynamical Systems and Symmetry*. Cambridge University Press.

HSU, M.-C. & BAZILEVS, Y. 2012 Fluid–structure interaction modeling of wind turbines: simulating the full machine. *Comput. Mech.* **50** (6), 821–833.

HURDAL, M.K., BOWERS, P.L., STEPHENSON, K., DE WITT, L.S., REHM, K., SCHAPER, K. & ROTTENBERG, D.A. 1999 Quasi-conformally flat mapping the human cerebellum. In *International Conference on Medical Image Computing and Computer-Assisted Intervention*, pp. 279–286. Springer.

JEUN, J., NICHOLS, J.W & JOVANOVIĆ, M.R. 2016 Input-output analysis of high-speed axisymmetric isothermal jet noise. *Phys. Fluids* **28** (4), 047101.

JØRGENSEN, B.H., SØRENSEN, J.N. & BRØNS, M. 2003 Low-dimensional modeling of a driven cavity flow with two free parameters. *Theor. Comput. Fluid Dyn.* **16** (4), 299–317.

KAMENSKY, D., HSU, M.-C., SCHILLINGER, D., EVANS, J.A., AGGARWAL, A., BAZILEVS, Y., SACKS, M.S. & HUGHES, T.J.R. 2015 An immersogeometric variational framework for fluid–structure interaction: application to bioprosthetic heart valves. *Comput. Meth. Appl. Mech. Engng* **284**, 1005–1053.

KEHOE, M.W. 1995 A historical overview of flight flutter testing. *NASA Tech. Rep. 4720. NASA*.

KERN, S. & KOUMOUTSAKOS, P. 2006 Simulations of optimized anguilliform swimming. *J. Expl Biol.* **209** (24), 4841–4857.

KOVALSKY, S.Z., AIGERMAN, N., BASRI, R. & LIPMAN, Y. 2015 Large-scale bounded distortion mappings. *ACM Trans. Graph.* **34** (6), 191.

KUTZ, J.N. 2013 *Data-Driven Modeling & Scientific Computation: Methods for Complex Systems & Big Data*. Oxford University Press.

KUTZ, J.N., FU, X. & BRUNTON, S.L. 2016 Multiresolution dynamic mode decomposition. *SIAM. J. Appl. Dyn. Syst.* **15** (2), 713–735.

LANATA, F. & DEL GROSSO, A. 2006 Damage detection and localization for continuous static monitoring of structures using a proper orthogonal decomposition of signals. *Smart Mater. Struct.* **15** (6), 1811.

LANG, S. 2012 *Fundamentals of Differential Geometry*, vol. 191. Springer Science & Business Media.

LEE, Y.T., LAM, K.C. & LUI, L.M. 2016 Landmark-matching transformation with large deformation via n-dimensional quasi-conformal maps. *J. Sci. Comput.* **67** (3), 926–954.

LeGresley, P. & Alonso, J. 2000 Airfoil design optimization using reduced order models based on proper orthogonal decomposition. In *Fluids 2000 Conference and Exhibit*, p. 2545. AIAA.

Lei, C., Cheng, L. & Kavanagh, K. 2000 A finite difference solution of the shear flow over a circular cylinder. *Ocean Engng* **27** (3), 271–290.

Li, H. & Hartley, R. 2007 Conformal spherical representation of 3D genus-zero meshes. *Pattern Recognit.* **40** (10), 2742–2753.

Liberge, E. & Hamdouni, A. 2010 Reduced order modelling method via proper orthogonal decomposition (POD) for flow around an oscillating cylinder. *J. Fluids Struct.* **26** (2), 292–311.

Lighthill, M.J. 1960 Note on the swimming of slender fish. *J. Fluid Mech.* **9** (2), 305–317.

Liu, H., Wassersug, R. & Kawachi, K. 1996 A computational fluid dynamics study of tadpole swimming. *J. Expl Biol.* **199** (6), 1245–1260.

Liu, J. & Hu, H. 2010 Biological inspiration: from carangiform fish to multi-joint robotic fish. *J. Bionic Engng* **7** (1), 35–48.

Lumley, J.L. 1967 The structure of inhomogeneous turbulent flows. In *Atmospheric Turbulence and Radio Wave Propagation* (ed. A.M. Yaglom & V.I. Tatarsky). Nauka.

Ly, H.V. & Tran, H.T. 2001 Modeling and control of physical processes using proper orthogonal decomposition. *Math. Comput. Model.* **33** (1–3), 223–236.

Maertens, A.P., Gao, A. & Triantafyllou, M.S. 2017 Optimal undulatory swimming for a single fish-like body and for a pair of interacting swimmers. *J. Fluid Mech.* **813**, 301–345.

Marchese, A.D., Onal, C.D. & Rus, D. 2014 Autonomous soft robotic fish capable of escape maneuvers using fluidic elastomer actuators. *Soft Robot.* **1** (1), 75–87.

Mariappan, S., Gardner, A., Richter, K. & Raffel, M. 2013 Analysis of dynamic stall using dynamic mode decomposition technique. In *31st AIAA Applied Aerodynamics Conference*, p. 3040. AIAA.

Marsden, J.E. 1981 *Lectures on Geometric Methods in Mathematical Physics*. SIAM.

Martín-Alcántara, A., Fernandez-Feria, R. & Sanmiguel-Rojas, E. 2015 Vortex flow structures and interactions for the optimum thrust efficiency of a heaving airfoil at different mean angles of attack. *Phys. Fluids* **27** (7), 073602.

McKeon, B.J., Sharma, A.S. & Jacobi, I. 2013 Experimental manipulation of wall turbulence: a systems approach. *Phys. Fluids* **25** (3), 031301.

Menon, K. & Mittal, R. 2020*a* Dynamic mode decomposition based analysis of flow over a sinusoidally pitching airfoil. *J. Fluids Struct.* **94**, 102886.

Menon, K. & Mittal, R. 2020*b* On the initiation and sustenance of flow-induced vibration of cylinders: insights from force partitioning. arXiv:2006.11649.

Mezić, I. 2013 Analysis of fluid flows via spectral properties of the Koopman operator. *Annu. Rev. Fluid Mech.* **45**, 357–378.

Michelin, S., Smith, S.G.L. & Glover, B.J. 2008 Vortex shedding model of a flapping flag. *J. Fluid Mech.* **617**, 1–10.

Mittal, R. & Iaccarino, G. 2005 Immersed boundary methods. *Annu. Rev. Fluid Mech.* **37**, 239–261.

Moghaddam, B. & Pentland, A. 1995 Probabilistic visual learning for object detection. In *Proceedings of IEEE International Conference on Computer Vision*, pp. 786–793. IEEE.

Morgan, H.L. Jr.2002 Experimental test results of energy efficient transport (EET) high-lift airfoil in langley low-turbulence pressure tunnel. NASA.

Moriche, M., Flores, O. & García-Villalba, M. 2017 On the aerodynamic forces on heaving and pitching airfoils at low Reynolds number. *J. Fluid Mech.* **828**, 395–423.

Noack, B.R., Afanasiev, K., Morzyński, M., Tadmor, G. & Thiele, F. 2003 A hierarchy of low-dimensional models for the transient and post-transient cylinder wake. *J. Fluid Mech.* **497**, 335–363.

Ojima, A. & Kamemoto, K. 2005 Numerical simulation of unsteady flows around a fish. In *Proceedings of ICVFM*, pp. 21–23.

Paillé, G.-P. & Poulin, P. 2012 As-conformal-as-possible discrete volumetric mapping. *Comput. Graph.* **36** (5), 427–433.

Pozrikidis, C. 2011 *Introduction to Theoretical and Computational Fluid Dynamics*. Oxford University Press.

Ravindran, S.S. 2000 A reduced-order approach for optimal control of fluids using proper orthogonal decomposition. *Intl J. Numer. Meth. Fluids* **34** (5), 425–448.

Roshko, A. 1961 Experiments on the flow past a circular cylinder at very high Reynolds number. *J. Fluid Mech.* **10** (3), 345–356.

Roweis, S.T. 1998 EM algorithms for PCA and SPCA. In *Advances in Neural Information Processing Systems*, pp. 626–632. MIT Press.

ROWLEY, C.W., COLONIUS, T. & MURRAY, R.M. 2004 Model reduction for compressible flows using POD and Galerkin projection. *Physica* D **189** (1–2), 115–129.

ROWLEY, C.W., MEZIĆ, I., BAGHERI, S., SCHLATTER, P. & HENNINGSON, D.S. 2009 Spectral analysis of nonlinear flows. *J. Fluid Mech.* **641**, 115–127.

SAFFMAN, P.G. 1992 *Vortex Dynamics*. Cambridge University Press.

SAIKI, E.M. & BIRINGEN, S. 1996 Numerical simulation of a cylinder in uniform flow: application of a virtual boundary method. *J. Comput. Phys.* **123** (2), 450–465.

SCHMID, P.J. 2010 Dynamic mode decomposition of numerical and experimental data. *J. Fluid Mech.* **656**, 5–28.

SCHMIDT, O.T. & COLONIUS, T. 2020 Guide to spectral proper orthogonal decomposition. *AIAA J.* **58** (3), 1023–1033.

SFAKIOTAKIS, M., LANE, D.M. & DAVIES, J.B.C. 1999 Review of fish swimming modes for aquatic locomotion. *IEEE J. Ocean. Engng* **24** (2), 237–252.

SHOELE, K. & ZHU, Q. 2015 Drafting mechanisms between a dolphin mother and calf. *J. Theor. Biol.* **382**, 363–377.

SIEBER, M., PASCHEREIT, C.O. & OBERLEITHNER, K. 2016 Spectral proper orthogonal decomposition. *J. Fluid Mech.* **792**, 798–828.

SIROVICH, L. 1987 Turbulence and the dynamics of coherent structures. I. Coherent structures. *Q. Appl. Maths* **45** (3), 561–571.

SPAGNOLIE, S.E. & SHELLEY, M.J. 2009 Shape-changing bodies in fluid: hovering, ratcheting, and bursting. *Phys. Fluids* **21** (1), 013103.

STEELE, S.C., WEYMOUTH, G.D. & TRIANTAFYLLOU, M.S. 2017 Added mass energy recovery of octopus-inspired shape change. *J. Fluid Mech.* **810**, 155–174.

TADMOR, G., BISSEX, D., NOACK, B., MORZYNSKI, M., COLONIUS, T. & TAIRA, K. 2008 Temporal-harmonic specific POD mode extraction. In *4th Flow Control Conference*, p. 4190. AIAA.

TAIRA, K., BRUNTON, S.L., DAWSON, S.T.M., ROWLEY, C.W., COLONIUS, T., MCKEON, B.J., SCHMIDT, O.T., GORDEYEV, S., THEOFILIS, V. & UKEILEY, L.S. 2017 Modal analysis of fluid flows: an overview. *AIAA J.* **55** (12), 1–29.

TAKIZAWA, K., HENICKE, B., PUNTEL, A., SPIELMAN, T. & TEZDUYAR, T.E. 2012 Space-time computational techniques for the aerodynamics of flapping wings. *J. Appl. Mech.* **79** (1), 010903.

TAYLOR, G.I. 1953 Formation of a vortex ring by giving an impulse to a circular disk and then dissolving it away. *J. Appl. Phys.* **24** (1), 104–104.

TAYLOR, J.A. & GLAUSER, M.N. 2004 Towards practical flow sensing and control via POD and LSE based low-dimensional tools. *Trans. ASME: J. Fluids Engng* **126** (3), 337–345.

THEOFILIS, V. 2011 Global linear instability. *Annu. Rev. Fluid Mech.* **43**, 319–352.

TIPPING, M.E. & BISHOP, C.M. 1999 Probabilistic principal component analysis. *J. R. Stat. Soc.* B **61** (3), 611–622.

TOWNE, A., SCHMIDT, O.T. & COLONIUS, T. 2018 Spectral proper orthogonal decomposition and its relationship to dynamic mode decomposition and resolvent analysis. *J. Fluid Mech.* **847**, 821–867.

TRIANTAFYLLOU, M.S. & TRIANTAFYLLOU, G.S. 1995 An efficient swimming machine. *Sci. Am.* **272** (3), 64–70.

TROSHIN, V., SEIFERT, A., SIDILKOVER, D. & TADMOR, G. 2016 Proper orthogonal decomposition of flow-field in non-stationary geometry. *J. Comput. Phys.* **311**, 329–337.

TU, J.H., ROWLEY, C.W., LUCHTENBURG, D.M., BRUNTON, S.L. & KUTZ, J.N. 2014 On dynamic mode decomposition: theory and applications. *J. Comput. Dyn.* **1**, 391.

TYTELL, E.D., HSU, C.-Y., WILLIAMS, T.L., COHEN, A.H. & FAUCI, L.J. 2010 Interactions between internal forces, body stiffness, and fluid environment in a neuromechanical model of lamprey swimming. *Proc. Natl Acad. Sci.* **107** (46), 19832–19837.

UKEILEY, L., CORDIER, L., MANCEAU, R., DELVILLE, J., GLAUSER, M. & BONNET, J.P. 2001 Examination of large-scale structures in a turbulent plane mixing layer. Part 2. Dynamical systems model. *J. Fluid Mech.* **441**, 67–108.

VERCAUTEREN, T., PENNEC, X., PERCHANT, A. & AYACHE, N. 2007 Non-parametric diffeomorphic image registration with the demons algorithm. In *International Conference on Medical Image Computing and Computer-Assisted Intervention*, pp. 319–326. Springer.

VIDELER, J.J. & HESS, F. 1984 Fast continuous swimming of two pelagic predators, saithe (pollachius virens) and mackerel (scomber scombrus): a kinematic analysis. *J. Expl Biol.* **109** (1), 209–228.

VIDELER, J.J. 2012 *Fish Swimming*. Springer Science & Business Media.

WANG, Z.J. 2000 Vortex shedding and frequency selection in flapping flight. *J. Fluid Mech.* **410**, 323–341.

WANG, Z.J., BIRCH, J.M. & DICKINSON, M.H. 2004 Unsteady forces and flows in low Reynolds number hovering flight: two-dimensional computations vs robotic wing experiments. *J. Expl Biol.* **207** (3), 449–460.

WANG, T.-K. & SHOELE, K. 2018 Aeroelastic flutter in the presence of an active flap. In *2018 Fluid Dynamics Conference*, p. 3089. AIAA.

WANG, Y., *et al.* 2003 Volumetric harmonic map. *Commun. Inf. Syst.* **3** (3), 191–202.

WASSERSUG, R.J. & VON SECHENDORF HOFF, K. 1985 The kinematics of swimming in anuran larvae. *J. Expl Biol.* **119** (1), 1–30.

WEBB, P.W. 1971 The swimming energetics of trout: II. Oxygen consumption and swimming efficiency. *J. Expl Biol.* **55** (2), 521–540.

WEYMOUTH, G.D. & TRIANTAFYLLOU, M.S. 2012 Global vorticity shedding for a shrinking cylinder. *J. Fluid Mech.* **702**, 470–487.

WU, T.Y.-T. 1971 Hydromechanics of swimming propulsion. Part 1. Swimming of a two-dimensional flexible plate at variable forward speeds in an inviscid fluid. *J. Fluid Mech.* **46** (2), 337–355.

WU, J., LIU, L. & LIU, T. 2018 Fundamental theories of aerodynamic force in viscous and compressible complex flows. *Prog. Aerosp. Sci.* **99**, 27–63.

YANUSHAUSKAS, A. 1970 On harmonic mappings of three dimensional domains. *Siber. Math. J.* **11** (4), 684–696.

YU, J., TAN, M., WANG, S. & CHEN, E. 2004 Development of a biomimetic robotic fish and its control algorithm. *IEEE Trans. Syst. Man Cybern.* B **34** (4), 1798–1810.

ZENG, W. & GU, X.D. 2011 Registration for 3D surfaces with large deformations using quasi-conformal curvature flow. In *CVPR 2011*, pp. 2457–2464. IEEE.

ZHANG, C., HEDRICK, T.L. & MITTAL, R. 2015 Centripetal acceleration reaction: an effective and robust mechanism for flapping flight in insects. *PloS One* **10** (8), e0132093.

ZHANG, H., ROWLEY, C.W., DEEM, E.A. & CATTAFESTA, L.N. 2019 Online dynamic mode decomposition for time-varying systems. *SIAM J. Appl. Dyn. Syst.* **18** (3), 1586–1609.

ZHAO, M., CHENG, L., TENG, B. & LIANG, D. 2005 Numerical simulation of viscous flow past two circular cylinders of different diameters. *Appl. Ocean Res.* **27** (1), 39–55.

ZHU, Q. & PENG, Z. 2009 Mode coupling and flow energy harvesting by a flapping foil. *Phys. Fluids* **21** (3), 033601.